Downloaded by [Shenzhen University Town] at 19:33 15 August 2011

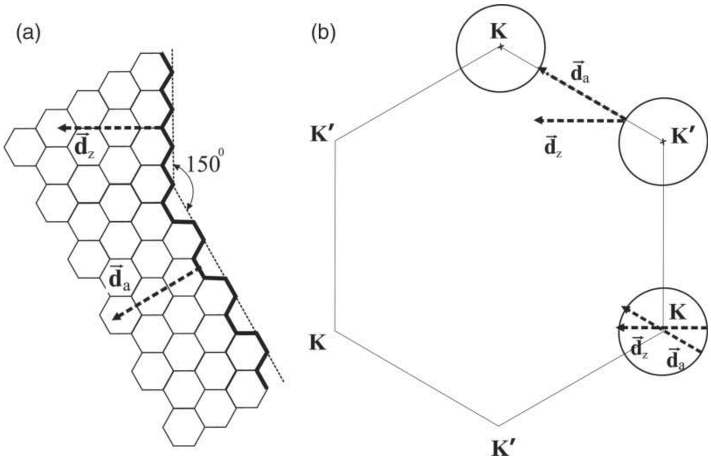

Figure 50. (a) Schematic illustration of the atomic structure of edges with the zigzag and armchair orientations. The boundaries can scatter electrons with momentum transfer along $\vec{\mathbf{d}}_z$ for the zigzag edge, and along $\vec{\mathbf{d}}_a$ for the armchair edge. (b) First BZ of 2D graphite (graphene), showing defect-induced inter-valley and intra-valley scattering processes. Since $\vec{\mathbf{d}}_z$ is too short to connect the K and K' points, the defect-induced DR inter-valley process is forbidden at zigzag edges. Reprinted figure with permission from L.G. Cancado *et al.*, Physical Review B 93, p. 47403, 2004 [59]. Copyright © (2004) by the American Physical Society.

the specific defect structure on the Raman spectra of sp^2 carbon systems. Other defect-dependent effects are expected, which may be very useful to characterize defects in nanographite-based devices, but both theory and experiment have to be developed along these lines.

4.5. *Polarization effects in graphene nanoribbons*

Polarization effects have also been observed in the G-band of graphene nanoribbons, as shown in Figure 51 [59]. Again, this development came before the graphene rush, and the experimental results were actually obtained on a one-layer thick ribbon grown by CVD on top of HOPG. The lower frequency G_1 band in Figure 51 comes from the nano-ribbon, while the higher frequency G_2 band comes from the HOPG substrate. The reason why the frequencies are distinct is actually related to the different heat dissipation, whereby the nano-ribbon and the substrate get into equilibrium at different temperatures when heated independently by the laser (see Figure 51). Thus the nanoribbon is heated to a higher temperature by the laser heating than the substrate, and therefore ω_{G_1} for the nanoribbon decreases more than ω_{G_2} for the substrate. This happens because the thermal conductivity of the substrate is much higher than that of the graphene ribbon, as shown in Figure 51(c).

Finally, the nanoribbon G_1 band shows a clear dependence on the excitation laser light polarization with respect to its axis, as illustrated in Figure 51(b). The Raman signal for the ribbon disappears when the light polarization direction is perpendicular to the ribbon axis. This result is related to both the anisotropy of the optical absorption (emission), according to Equation (82), and the quantum confinement perpendicular to the ribbon axis.

Downloaded by [Shenzhen University Town] at 19:33 15 August 2011

5. Raman spectra of carbon nanotubes

Since the Raman spectra of carbon nanotubes have additional unique spectral features that are not found in other carbon nano-structured materials, Raman spectroscopy has provided an especially important tool for developing characterization techniques for nanocarbon materials [313]. In particular the RBM, which is unique to carbon nanotubes (see Figure 4), provides a highly sensitive tool for determining the presence of carbon nanotubes in a particular carbon-based sample and for characterizing the (n, m) chirality of the carbon nanotubes present in the sample. The KA effect provides a mechanism for study of the el–ph interaction through its effect on both the G-band and the RBM mode features in the Raman spectra. The DR effect provides a mechanism for studying aspects of the 1D quantum confined electronic energy band structure through the el–ph interaction. Since the electronic transitions in carbon nanotubes are dominated by excitonic effects, study of the Raman spectra of carbon nanotubes provides important insights into excitonic phenomena in 1D systems. Near-field Raman spectroscopy has been especially sensitive for revealing new and important spatial information about specific defects in carbon nanotubes. These topics are discussed in this Section.

5.1. *The radial breathing mode and the Kataura plot*

The RBM is the nanotube normal mode vibration where all the C atoms vibrate in phase in the radial direction, as if the tube is breathing. Since the atomic vibrational motion does not break the tube symmetry, the RBM is a totally symmetric mode according to group theory, belonging to the A_1 symmetry irreducible representation (IR) [1,141,142]. The RBM only occurs in carbon

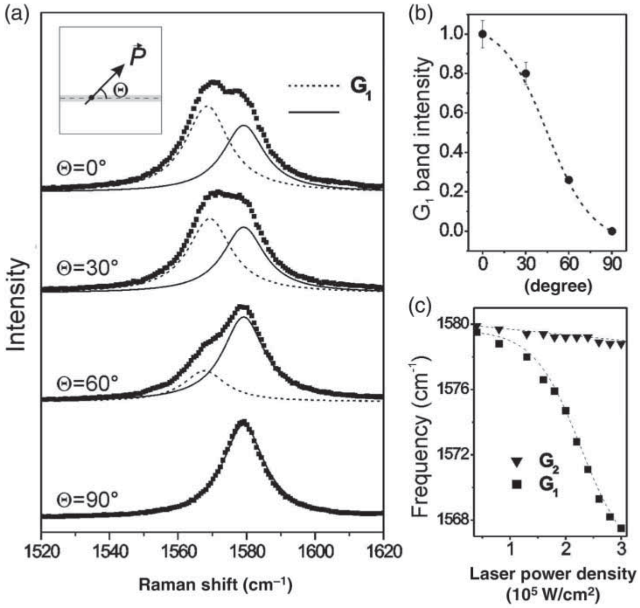

Figure 51. (a) The G-band Raman spectra from a graphene nano-ribbon (G_1) and from the HOPG substrate (G_2) on which the nano-ribbon was grown. (b) The dependence of the G_1 frequency on the light polarization direction, with respect to the ribbon axis. Points are experimental results and the dashed curve is the theoretical expectation. (c) Frequency of the G_1 and G_2 peaks as a function of the incident laser power density. Reprinted figure with permission from L.G. Cancado *et al.*, Physical Review B 93, p. 47403, 2004 [59]. Copyright © (2004) by the American Physical Society.

Downloaded by [Shenzhen University Town] at 19:33 15 August 2011

nanotubes and, therefore, it can be used to distinguish SWNTs from other sp^2 carbon structures in the samples. In general the intensity of the RBM is unusually strong when compared with other non-resonant spectral features coming from other carbonaceous materials or from the substrate on which the tubes are sitting [111]. Furthermore, the RBM frequency ω_{RBM} depends on the tube diameter, following the proportionality relation $\omega_{\mathrm{RBM}} \propto 1/d_t$. This dependence was predicted initially using force constant calculation models (e.g. [100]), but a rather simple and instructive analytical derivation can be made using elasticity theory, and we present this approach in sequence.

5.1.1. *The RBM frequency*

The RBM frequency of a SWNT is given by $\omega_{\mathrm{RBM}} = A/d_t$, with the value $A = 227\,\mathrm{cm}^{-1}\mathrm{nm}$ being expected by elasticity theory, thereby directly connecting 1D carbon nanotubes to their 2D counterpart graphene from which nanotubes are conceptually derived [314,315]. The experimental values for A and the expected value for A coming from elasticity theory agree perfectly for one specific type of SWNT [314,315], that is, for SWNTs which are ultra-long, vertically aligned, and grown by the water-assisted CVD method [316]. This sp^2 carbon material is used here as a standard reference material from a metrology standpoint. Most of the RBM experimental results in the literature have been fitted to the relation $\omega_{\mathrm{RBM}}=A/d_t+B$, with values for the parameters A and B varying widely from paper to paper [107,109,111,153,175,188,314,317–321]. In the limit of the tube diameter going to infinity, we ideally expect $\omega_{\mathrm{RBM}} \to 0$, suggesting that B is associated with an environmental effect, and the environmental conditions differ from one experimental system to another.

A simple model that has been used to model the RBM is a simple harmonic oscillator equation for a cylindrical shell subjected to an inwards pressure ($p(x)$) given by [314,315]

$$\frac{\rho}{Y}(1-\nu^2)\frac{\partial^2 x(t)}{\partial t^2} + \frac{2}{d_t}x(t) = -\frac{(1-\nu^2)}{Yh}p(x), \tag{83}$$

where $x(t)$ is the displacement of the nanotube in the radial direction, $p(x) = (24K/s_0^2)x(t)$, and K (in eV/Å^2) gives the van der Waals interaction strength, s_0 the equilibrium separation between the SWNT wall and the surrounding environmental shell, Y the Young's modulus (69.74×10^{11} g/cm·s^2), ρ the mass density per unit volume (2.31 gm/cm^3), $\nu = 0.5849$ is the Poisson's ratio and h represents the thickness of the environmental shell [315]. If there are no environmental effects, the term $p(x)$ vanishes and Equation (83) will become the fundamental frequency ω^0_{RBM} for a pristine SWNT in units of cm^{-1},

$$\omega^0_{\mathrm{RBM}} = \left\{\frac{1}{\pi c}\left[\frac{Y}{\rho(1-\nu^2)}\right]^{1/2}\right\}\frac{1}{d_t}. \tag{84}$$

The term inside the curly bracket above gives the fundamental value of $A = 227.0\,\mathrm{cm}^{-1}\mathrm{nm}$. However, for a non-vanishing inward pressure $p(x)$, the result is

$$\omega'_{\mathrm{RBM}} = 227.0\left[\frac{1}{d_t^2} + \frac{6(1-\nu^2)}{Yh}\frac{K}{s_0^2}\right]^{1/2}. \tag{85}$$

Here $[6(1-\nu^2)/Yh] = 26.3\,\text{Å}^2/\mathrm{eV}$. The shift in ω'_{RBM} due to the nanotube environment is given by $\Delta\omega_{\mathrm{RBM}} = \omega'_{\mathrm{RBM}} - \omega^0_{\mathrm{RBM}}$. We fit the value K/s_0^2 in Equation (3) to the RBM frequency as a function of d_t. The fitted value for the environmental term for the "super-growth" sample is sufficiently small, since $K/s_0^2 = (2.2 \pm 0.1)\,\mathrm{meV}/\text{Å}^4$, that it can be neglected. The d_t dependent

Table 2. Environmental effects on the RBM frequency of different samples, as measured by the C_e factor in Equation (86) [323].

C_e	Sample	Reference
0	Water-assisted CVD	Araujo [314]
0.05	HiPCO@SDS	Bachilo [153]
0.059	Alcohol-assisted CVD	Araujo [321]
0.065	SWNT@SiO$_2$	Jorio [111]
0.067	Free-standing	Paillet [320]

behavior of the environmental effect in ω_{RBM} reproduces well the experimental result for d_t up to $d_t = 3\,\mathrm{nm}$ [314]. A similar environmental effect is obtained for SWNTs surrounded by different surfactants [107,175,188,317,319], in bundles [109,321], sitting on a SiO$_2$ substrate [111], and even for tubes suspended in air by posts [320]. This environmental effect is almost absent in “super-growth” SWNTs, but the reason why this sample is special is not presently understood, and the pristine-like ω_{RBM} behavior is lost if this sample is dispersed in solution [322].

A simple relation can be proposed for all the ω_{RBM} results in the literature, which are generally upshifted from the pristine values observed for the “super-growth” samples due to the van der Waals interaction with the environment. This simple relation is [314]

$$\omega_{\mathrm{RBM}}^{\mathrm{Lit.}} = \frac{227}{d_t}\sqrt{1 + C_e * d_t^2}, \tag{86}$$

where C_e in Equation (86) represents the effect of the environment on ω_{RBM}, i.e. $C_e = [6(1-\nu^2)/Eh][K/s_0^2]\,\mathrm{nm}^{-2}$. The several C_e values that are obtained by fitting the RBM results for different commonly found samples in the literature are given in Table 2. The curvature effects become important for $d_t < 1.2\,\mathrm{nm}$, and in this case the environmental effect depends more critically on the specific sample. For example, the C_e for SWNT samples sitting on a SiO$_2$ substrate may differ from sample to sample. The observed environmentally induced upshifts for the RBM from small diameter tubes, either within bundles or wrapped by different surfactants (e.g., SDS (sodium dodecyl sulfate) or single stranded DNA), range from 1 to 10 cm^{-1}. This environmental effect gets richer in a double wall carbon nanotube (DWNT), as discussed in Section 5.1.2.

Finally, all the ω_{RBM} dependence on the carbon nanotube structure discussed here addresses the importance of the diameter dependence. The chiral angle has a weaker dependence on the RBM frequency, but to fully discuss this topic, the KA has to be introduced [193,324]. This topic is discussed in Section 5.4.

5.1.2. *The RBM for double wall carbon nanotubes*

Spectroscopic experiments on DWNTs have been largely performed on solution-based samples or in bundles [325–329]. For this reason, it has been difficult to identify and learn about the Raman spectroscopic signatures that are specific to the inner (n, m) tube of a DWNT, which can be contained inside different possible outer (n', m') tubes (see Figure 52(a)). The DWNTs are formed by an inner and an outer tube, and they can be either metallic (M) or semiconducting (S). There are four different possible configurations, namely M@M, M@S, S@S and S@M. Here S@M denotes a DWNT with an S inner tube inside an M outer tube, following a similar notation introduced for fullerenes [330,331]. Interesting aspects are related to the DWNT electronic properties, e.g. the S@M configuration can be regarded as a good approximation for an isolated semiconducting SWNT, since it is electrostatically shielded by the outer metallic tube [330]. In order to determine

Downloaded by [Shenzhen University Town] at 19:33 15 August 2011

which specific inner and outer tubes form a given DWNT, one has to perform Raman experiments on individual DWNTs (see Figure 52(c)).

For a well-defined experiment, the combination of electron-beam lithography, atomic force microscopy (AFM) and Raman spectral mapping have been developed to measure the Raman spectra from the inner and the outer tubes of an individual DWNT (see Figure 52) [330,331]. The Raman spectra of 11 isolated DWNTs grown from annealing C_{60} filled SWNTs were measured using a single laser excitation energy ($E_{\text{laser}} = 2.10$ eV [330]).Specific E_{laser} values were used to select all DWNTs with (6,5) semiconducting inner tubes that were in resonance, and all with the S@M configuration so that the RBMs from both the inner and outer tubes of individual DWNTs could be observed. The RBM frequencies $\omega_{\text{RBM},o}$ for the outer tube measured for such a DWNT as a function of $\omega_{\text{RBM},i}$ for the inner tube are shown in Figure 53(a). For these 11 individual isolated DWNTs, $\omega_{\text{RBM},o}$ for the outer tubes varies along with $\omega_{\text{RBM},i}$, thus showing that the inner and outer tubes impose considerable stress on one another. Actually, the nominal wall-to-wall distances $\Delta d_{t,io}$ between the inner (i) and outer (o) tubes of the DWNTs are less than the 0.335 nm interlayer c-axis distance in graphite. Figure 53(b) shows $\Delta d_{t,io}$ values as small as 0.29 nm, with a decrease of up to 13% in the wall to wall distance [330]. Because of the differences in the Coulomb interaction

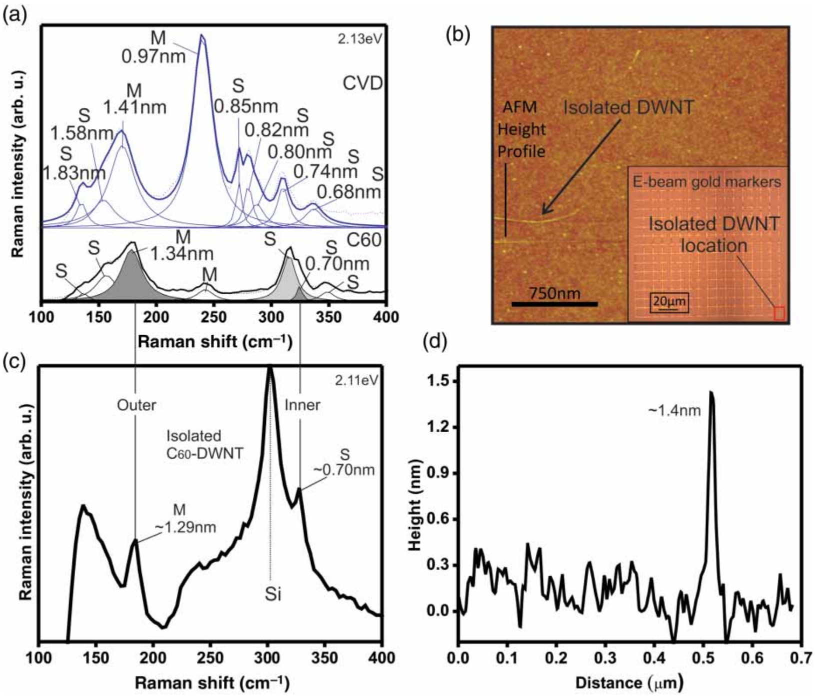

Figure 52. (a) Raman spectra for the RBM region for two types of DWNTs, obtained with $E_{\text{laser}} = 2.13$ eV. (b) AFM image of one individual DWNT. The inset shows the silicon substrate with gold markers showing the location of an individual DWNT. (c) RBM Raman spectra obtained with $E_{\text{laser}} = 2.11$ eV for an isolated individual DWNT grown from a C_{60} filled SWNT-bundle. (d) AFM height profile of the individual, isolated DWNT shown in (b), with the RBM spectrum shown in (c). The vertical lines connecting (a) and (c) show that the ω_{RBM} of the prominent tube diameters observed in the C_{60}-DWNT bundles coincide with the ω_{RBM} of the inner and outer tubes of the isolated C_{60}-DWNT. F. Villalpando-Paez *et al.*, Nanoscale 2, pp. 406–411, 2010 [330]. Adapted by permission of the Royal Society of Chemistry.

Downloaded by [Shenzhen University Town] at 19:33 15 August 2011

Downloaded by [Shenzhen University Town] at 19:33 15 August 2011

expected for the four different DWNT metallicity configurations, S@M, M@S, S@S and M@M, the detailed relation between $\omega_{\rm RBM}$ and $1/d_t$ will depend on the metallicity configuration.

By adding walls to form MWNTs, the RBM signal from inner tubes with small enough diameters ($d_t \lesssim 2\,{\rm nm}$) can be observed experimentally [332]. However, most of the usually made MWNT samples are composed of inner tubes with diameters too large to exhibit observable RBM features.

5.1.3. *The Raman excitation profile for the RBM*

In the Raman scattering experiment, when the energy of the incident or scattered light matches an optical transition in the scattering system, resonance effects occur, and the Raman signal is strongly enhanced [103,109,111]. Using the resonance Raman effect, it is possible to study the electronic structure of individual SWNTs [111,336,338]. In this section, we review observations of the Raman excitation profile for the RBM feature for an individual SWNT.

Isolated SWNTs were grown on top of a Si/SiO$_2$ substrate by a CVD method [111,339]. Figure 54(a) shows an AFM image of the substrate with lithographic markers that were used to locate an individual SWNT. The dashed circles in Figure 54(a,b) display the position where the laser spot is placed. Figure 54(c,d) show anti-Stokes/Stokes Raman spectra of the sample, measured in the excitation wavelength (energy) range $1.585\,{\rm eV} \le E_{\rm laser} \le 1.722\,{\rm eV}$. The Stokes/anti-Stokes ratio are calibrated by $[n(\omega)+1]/n(\omega)$, where $n(\omega) = 1/[\exp(\hbar\omega/k_{\rm B}T) - 1]$, ω is the RBM frequency, $k_{\rm B}$ is the Boltzmann constant, and T is the temperature, which was found not to be higher than 325 K [338].

An RBM Raman feature appears in the spectra in Figure 54(c,d) at $173.6\,{\rm cm}^{-1}$, with a clear resonance behavior. The RBM peak appears and disappears over the tunable energy range of $E_{\rm laser}$, meaning that $E_{\rm laser}$ is tuned over the whole resonance window of one optical transition energy ($E_{\rm ii}$) for the SWNT which is sitting under the laser spot. The linewidth for the RBM peak is sharp, ($\Gamma_{\rm RBM} = 5\,{\rm cm}^{-1}$), showing a typical value measured for isolated SWNTs deposited on substrates [111,340]. Figure 55 shows the $173.6\,{\rm cm}^{-1}$ RBM peak intensity vs. $E_{\rm laser}$ for (a) the anti-Stokes and (b) Stokes processes for the individual SWNT measured in Figure 54.

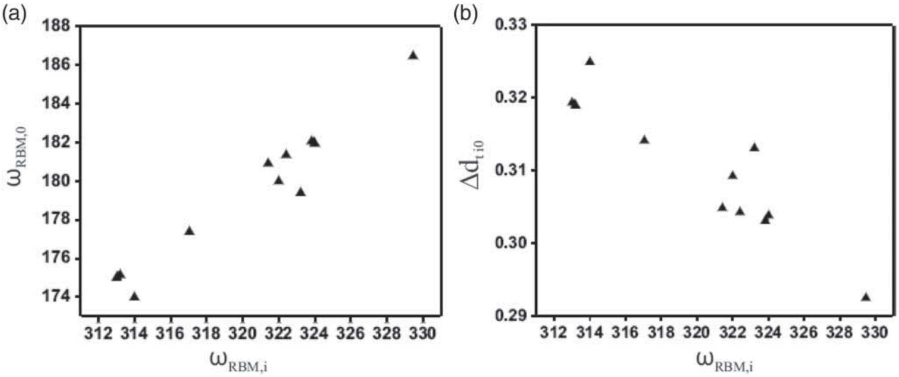

Figure 53. All the inner tubes for the 11 peapod-DWNTs in this figure are (6,5) semiconducting tubes. (a) Plot of the $\omega_{{\rm RBM},i}$ for the inner tube vs. $\omega_{{\rm RBM},o}$ for the outer tubes which pair to form eleven different isolated DWNTs. (b) Plot of the nominal wall-to-wall distance $\Delta d_{t,io}$ for each of the 11 isolated DWNTs vs. $\omega_{{\rm RBM},i}$ shown in (a). An increase in the $\omega_{{\rm RBM},i}$ of the (6,5) inner tubes shown here is accompanied by a decrease in the measured nominal wall-to-wall $d_{t,io}$ distance for these peapod-derived DWNTs. F. Villalpando-Paez *et al.*, Nanoscale 2, pp. 406–411, 2010 [330]. Adapted by permission of the Royal Society of Chemistry.

Downloaded by [Shenzhen University Town] at 19:33 15 August 2011

The Stokes RBM peak intensity I is a function of E_{laser} and can be evaluated from Equation (62) [269]. The two factors in the denominator of Equation (62) describe the resonance effect with the incident and scattered light, respectively. A ± sign before E_{ph} applies to Stokes/anti-Stokes processes, while γ_{RBM} is related to the inverse lifetime for the resonant scattering process [278]. The matrix elements in the numerator are most usually considered to be independent of energy because of the small energy range. The theory for these matrix elements is discussed in Section 3.6.1. The lines in Figure 55 show the fits to the experimental data for the Stokes (dashed) and anti-Stokes (solid) resonance windows, using $E_{\text{ph}} = 21.5\,\text{meV}$, obtained from $\omega_{\text{RBM}} = 173.6\,\text{cm}^{-1}$ [338]. The asymmetric lineshape in the resonance windows in Figure 55 was obtained in [338] by considering not a coherent Raman process, but an incoherent scattering process, where the sum over the internal states ($\sum_a$ in Equation (62)) was taken outside the square modulus. This procedure is indeed controversial because this asymmetry could be also generated by different γ_r values for the incident and scattered resonance windows or by other resonance levels lying close in energy.

Disregarding the asymmetry aspect, $E_{\text{ii}} = 1.655 \pm 0.003\,\text{eV}$ and $\gamma_{\text{RBM}} = 8\,\text{meV}$ is obtained for the spectra shown in Figure 55. A shift in the Stokes (S) and anti-Stokes (aS) resonant windows is expected due to the resonant condition for the scattered photon, $E_{\text{s}} = E_{\text{ii}} \pm E_{\text{ph}}$, with (+) for the Stokes and (−) for the anti-Stokes processes, and this effect is shown in the upper inset to Figure 55. For this reason, under sharp resonance conditions the $I_{\text{aS}}/I_{\text{S}}$ intensity ratio depends sensitively on $E_{\text{ii}} - E_{\text{laser}}$, and the $I_{\text{aS}}/I_{\text{S}}$ ratio can be used to determine E_{ii} experimentally and to determine whether the resonance is with the *incident* or the *scattered* photon [141,338].

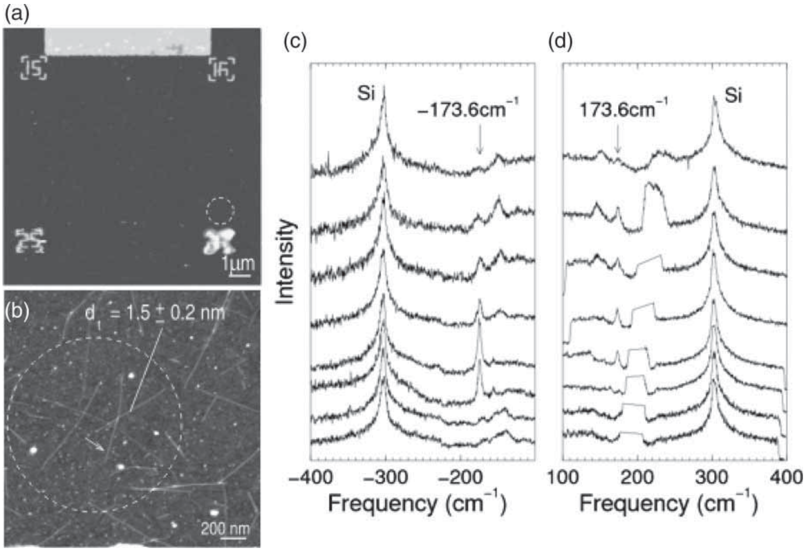

Figure 54. (a) AFM image of a SWNT sample showing markers that were used to localize the spot position (dashed circle) on the substrate during the Raman experiment and for further AFM characterization of the SWNTs that are located within the light spot indicated by the dashed circle in (b). (c) anti-Stokes and (d) Stokes Raman spectra from isolated SWNTs on a Si/SiO_2 substrate for several different laser excitation energies. For more details, see Ref. [338]. Adapted with permission from A. Jorio *et al.*, Physical Review B 63, p. 245416, 2001 [338]. Copyright © (2001) by the American Physical Society.

5.1.4. *The RBM spectra of SWNT bundles*

Figure 56(a) show a RBM Raman spectrum obtained from SWNT bundles [321]. The solid line shows the fit obtained using a sum of Lorentzians. Each Lorentzian gives the RBM from one specific (n, m) SWNT species. The red Lorentzians represent the RBM from metallic SWNTs

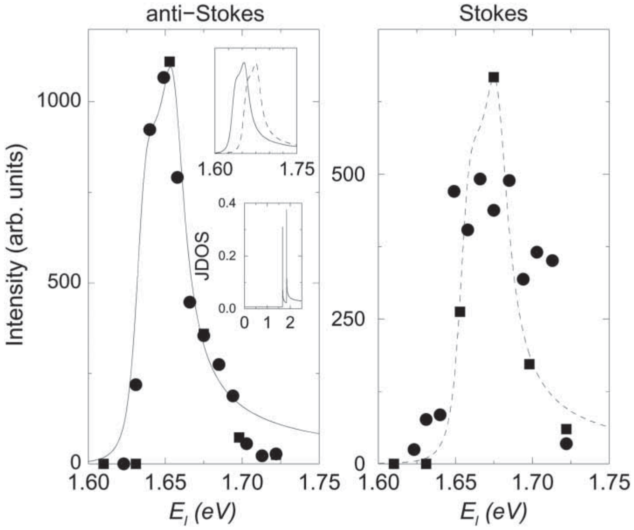

Figure 55. Raman intensity vs. laser excitation energy E_l for the $\omega_{\mathrm{RBM}} = 173.6\,\mathrm{cm}^{-1}$ peak in Figure 54, for both anti-Stokes and Stokes processes. Circles and squares indicate two different runs on the same sample. The line curves indicate the resonant Raman window predicted from Equation (1), with $E_{\mathrm{ii}} = 1.655\,\mathrm{eV}$, $\gamma_r = 8\,\mathrm{meV}$, but taking the sum over internal states $(\sum_{m,m'})$ outside the square modulus. The upper inset compares the theoretically predicted Stokes and anti-Stokes resonant windows on an energy scale in eV, and the lower insert shows the joint density of states (JDOS) vs. E_{laser} for this SWNT. Adapted with permission from A. Jorio *et al.*, Physical Review B 63, p. 245416, 2001 [338]. Copyright © (2001) by the American Physical Society.

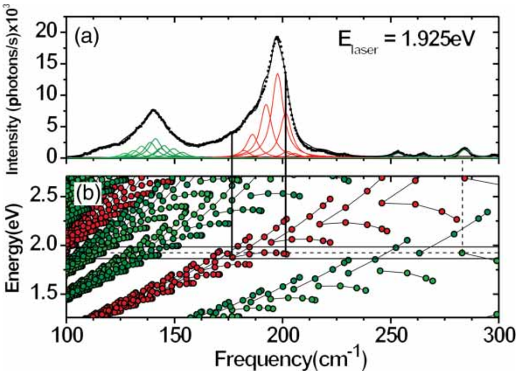

Figure 56. (a) Raman spectrum (bullets) of SWNT bundles obtained with a 644 nm laser line ($E_{\mathrm{laser}} = 1.925\,\mathrm{eV}$). This spectrum was fitted by using 34 Lorentzians (curves under the spectra) and the solid line is the fitting result. (b) The Kataura plot used as a guide for the fitting procedure. Adapted with permission from P.T. Araujo *et al.*, Physical Review Letters 98, p. 67401, 2007 [321]. Copyright © (2007) by the American Physical Society.

Downloaded by [Shenzhen University Town] at 19:33 15 August 2011

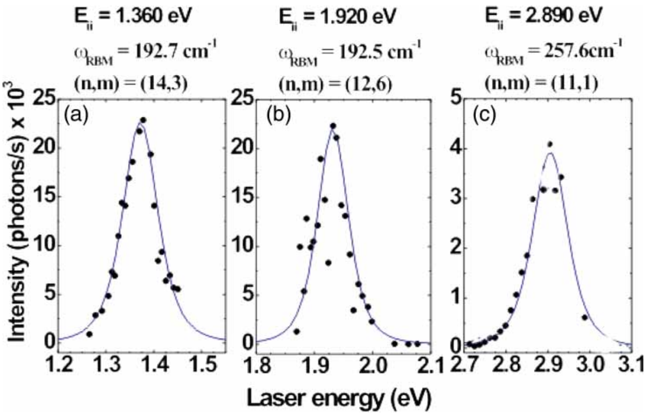

Figure 57. Resonance windows for specific (n,m) SWNTs within a bundle. (a) Resonance profile (black dots) in the near-infrared range for $\omega_{\mathrm{RBM}} = 192.7\,\mathrm{cm}^{-1}$. The data for tube $(14,3)$ were fitted (solid line) using Equation (87) with $\gamma = 0.065\,\mathrm{eV}$ and $E_{\mathrm{ii}} = 1.360\,\mathrm{eV}$. (b) Resonance profile in the visible range is shown for $\omega_{\mathrm{RBM}} = 192.5\,\mathrm{cm}^{-1}$ (tube $(12,6)$), with $\gamma = 0.045\,\mathrm{eV}$ and $E_{\mathrm{ii}} = 1.920\,\mathrm{eV}$. (c) Resonance profile in the near-ultraviolet range is shown for $\omega_{\mathrm{RBM}} = 257.6\,\mathrm{cm}^{-1}$ (tube $(11,1)$), with $\gamma = 0.073\,\mathrm{eV}$ and $E_{\mathrm{ii}} = 2.890\,\mathrm{eV}$. Adapted with permission from P.T. Araujo *et al.*, Physical Review Letters 98, p. 67401, 2007 [321]. Copyright © (2007) by the American Physical Society.

and the green Lorentzians represent the RBMs from semiconducting SWNTs. The number of Lorentzians used to fit each resonance spectrum can be defined by the Kataura plot [177,342,343] (see Figure 56(b)), which plots the E_{ii} for all possible (n,m) SWNTs. The ω_{RBM} values obey the relation $\omega_{\mathrm{RBM}} = (227/d_t)\sqrt{1 + C_e/d_t^2}$, which correctly describes environmental effects by the proper choice of C_e, and this relation is discussed in detail in Section 5.1.1. For lack of information, we assume that all the Lorentzian peaks in one experimental spectrum share the same FWHM value.

The RBM peak intensity $I(E_{\mathrm{laser}})$ for each Lorentzian peak in the RBM spectra from an individual SWNT can be evaluated by

$$I(E_{\mathrm{laser}}) \propto \left| \frac{1}{(E_{\mathrm{laser}} - E_{\mathrm{ii}} - \mathrm{i}\gamma)(E_{\mathrm{laser}} - E_{\mathrm{ii}} \pm E_{\mathrm{ph}} - \mathrm{i}\gamma)} \right|^2, \qquad (87)$$

which is a simplification of Equation (62). Figure 57 shows the resonance profiles for three different (n,m) SWNTs [321,335] The resonance window widths γ_r for SWNTs in bundles are usually within the 40–160 meV range, which are much broader than for isolated SWNTs (see Figure 55) and γ_r also depends on (n,m) [321].

5.1.5. (n,m) *dependence of RBM intensity – experimental analysis*

In experiments using a nearly continuous set of laser energies E_{L}, we compare the RBM intensity for different (n,m) SWNTs at a resonance condition (i.e., $E_{\mathrm{L}} = E_{\mathrm{ii}}$). The RBM spectra from the "super-growth" water-assisted SWNTs obey the relation $\omega_{\mathrm{RBM}} = 227/d_t\,\mathrm{cm}^{-1}\mathrm{nm}$ and these spectra have been used for (n,m)-dependent intensity analysis [344].

The d_t distribution of a given super-growth sample was established by high resolution transmission electron microscopy (HRTEM) [344], to calibrate the RRS (resonance Raman scattering) intensities. For the (n,m) analysis, it was assumed that SWNTs of different chiral angles are

Downloaded by [Shenzhen University Town] at 19:33 15 August 2011

Downloaded by [Shenzhen University Town] at 19:33 15 August 2011

equally abundant in the growth process. Actually, chiral SWNTs are twice as populous as achiral ones because there are right-handed and left-handed isomers present in a typical sample. The intensity calibrated experimental RRS map in shown in Figure 58(a). The (n, m) nanotubes in the $(2n + m) =$ constant family have similar diameters and E_{ii} values to one another, and the Raman intensity within a given $(2n + m) = p =$ constant family has a chiral angle dependence. From the spectral map it is clear that the RBM intensity is stronger for smaller chiral angles (near zigzag nanotubes) as compared to those with larger chiral angles. Each spectrum $(S_{(\omega,E_L),})$ is the sum of the individual contributions of all SWNTs present in the light beam, and we can write [344]

$$S_{(\omega,E_{\text{L}})} = \sum_{n,m}\left[\text{Pop}(n,m)I(n,m)^{E_{\text{L}}}\frac{\Gamma/2}{(\omega-\omega_{\text{RBM}})^2+(\Gamma/2)^2}\right], \tag{88}$$

where $\text{Pop}(n, m)$ is the relative population of the (n, m) nanotube species, $\Gamma = 3\,\text{cm}^{-1}$ is the experimental average value for the FWHM intensity of the Raman spectra (Lorentzian), ω_{RBM} is the RBM frequency and ω is the corresponding Raman shift variable. The total integrated area $(I(n, m)^{E_{\text{L}}})$ for the Stokes process at a given excitation laser energy (E_{L}) is given by

$$I(n,m)^{E_{\text{L}}} = \left|\frac{\mathcal{M}}{(E_{\text{L}}-E_{\text{ii}}+\text{i}\gamma)(E_{\text{L}}-E_{\text{ii}}-E_{ph}+\text{i}\gamma)}\right|^2, \tag{89}$$

where the superscript E_{L} denotes the laser excitation energy, $E_{\text{ph}} = \hbar\omega_{\text{RBM}}$ is the energy of the RBM phonon, E_{ii} is the energy corresponding to the ith excitonic transition, γ is the resonance window width and $\mathcal{M}$ represents the matrix elements for the Raman scattering by one RBM phonon of the (n, m) nanotube. The values for E_{ii} and ω_{RBM} have to be determined experimentally. The effective matrix element square term $\mathcal{M}$ and the effective resonance window width γ for each (n, m) tube were found by fitting the experimental RBM component of the RRS map with Equation (88) using the functions:

$$\mathcal{M} = \left[\mathcal{M}_{\text{A}} + \frac{\mathcal{M}_{\text{B}}}{d_t} + \frac{\mathcal{M}_{\text{C}}\cos(3\theta)}{d_t^2}\right]^2 \quad \text{and} \quad \gamma = \gamma_{\text{A}} + \frac{\gamma_{\text{B}}}{d_t} + \frac{\gamma_{\text{C}}\cos(3\theta)}{d_t^2}. \tag{90}$$

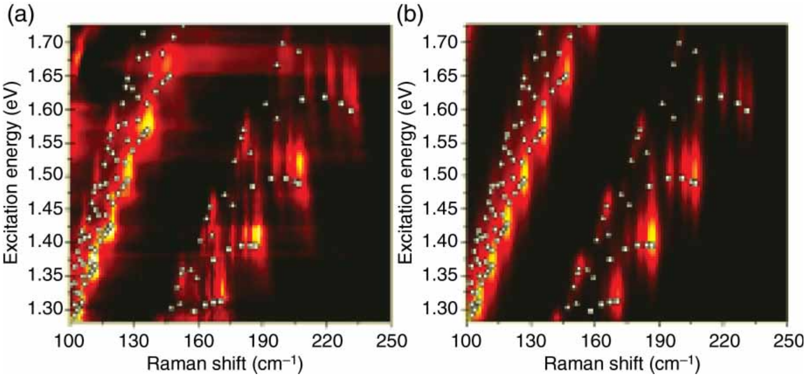

Figure 58. (a) Experimental RRS map for the RBM feature. The intensity calibration was made by measuring a standard tylenol sample. (b) Modeled map obtained by using Equation (88) in the same laser excitation energy range as (a). Adapted with permission from P.B.C. Pesce *et al.*, Applied Physical Letters 96, p. 51910, 2010 [344]. Copyright © (2010) by the American Institute of Physics.

Downloaded by [Shenzhen University Town] at 19:33 15 August 2011

Here $\mathcal{M}_i$ and γ_i ($i = \text{A}, \text{B}, \text{C}$) are fitting parameters. The best values for $\mathcal{M}_i$ and γ_i, considering the excitonic transitions E_{22}^S and the lower branch of E_{11}^M, are listed in Table 3. Here d_t is given in nm, γ in meV and $\mathcal{M}$ in arbitrary units.

The modeled RRS map shown in Figure 58(b) was obtained using the values thus obtained in Equation (88). Note that the model represents the experimentally observed results in Figure 58(a) very well.

5.1.6. *The experimental Kataura plot*

The resonance window analysis can be extended to all (n, m) SWNTs, from which we can study the E_{ii} dependence on (d_t, θ). Figure 59(a) shows a 2D RBM map for the "super-growth" (S.G.) SWNT sample [316]. The experimental Kataura plot in Figure 59(a) was constructed using 125 different laser excitation lines [314,335]. By applying the fitting procedure described in Section 5.1.4, the (n, m) indices have been assigned to 197 different SWNTs.

By fitting the resonance windows extracted from the data in Figure 59(a) as a function of $\omega_{\text{RBM}}^{S.G.}$, all $E_{\text{ii}}^{S.G.}$ excitonic transition energies have been obtained experimentally, as shown in Figure 59(b). These $E_{\text{ii}}^{S.G.}$ values displayed in Figure 59(b) have been fitted using the empirical equation [321,345]:

$$E_{\text{ii}}(p, d_t) = \alpha_p \frac{p}{d_t}\left[1 + 0.467 \log \frac{0.812}{p/d_t}\right] + \frac{\beta_p \cos 3\theta}{d_t^2}. \tag{91}$$

Here p is defined as $1, 2, 3, \ldots, 8$ for E_{11}^S, E_{22}^S, $E_{11}^M, \ldots, E_{66}^S$, and is a measure of the distance of each cutting line from the K point in the zone-folding procedure [135,177,343]. The fitting gives $\alpha_p = 1.074$ for $p = 1, 2, 3$ and $\alpha_p = 1.133$ for $p \geq 4$. The β_p values found for the lower (upper) E_{ii} branches are: $-0.07(0.09), -0.18(0.14), -0.19(0.29), -0.33(0.49), -0.43(0.59)$, $-0.6(0.57), -0.6(0.73)$ and -0.65 (unknown) for $p = 1, 2, 3, \ldots, 8$, respectively [335,345]. Equation (91) carries a linear dependence of E_{ii} on p/d_t, which is expected from tight-binding theory. It also includes a logarithmic correction term in p/d_t that comes from many-body interactions, plus a chiral angle θ dependence related to electronic trigonal warping and chirality-dependent curvature effects due to $\sigma - \pi$ hybridization [321]. The theoretical background for all these factors is discussed in Section 3.

5.2. ***Exciton environmental effect***

The E_{ii} values are now understood in terms of the bright exciton energy within the framework of a tight binding calculation which includes curvature optimization [254,346] and many-body effects [39–41,148,342]. The assignments of E_{ii} for SWNTs over a large region of both diameter ($0.7 < d_t < 3.8$ nm) and E_{ii} (1.2–2.7 eV) values and for a variety of surrounding materials are now available [21,230,335], thus making it possible to accurately determine the effect of the

Table 3. Adjusted parameters $\mathcal{M}_i$ and γ_i for metallic (M), semiconductor type 1 (S_1) and type 2 (S_2) tubes.

Type	$\mathcal{M}_\text{A}$	$\mathcal{M}_\text{B}$	$\mathcal{M}_\text{C}$	γ_A	γ_B	γ_C
M	1.68	0.52	5.54	23.03	28.84	1.03
S_1	−19.62	29.35	4.23	−3.45	65.10	7.22
S_2	−1.83	3.72	1.61	−10.12	42.56	−6.84

These parameters are to be used in Equation (90) with d_t in nm, yielding $\mathcal{M}$ in arbitrary units and γ in meV [344].

Downloaded by [Shenzhen University Town] at 19:33 15 August 2011

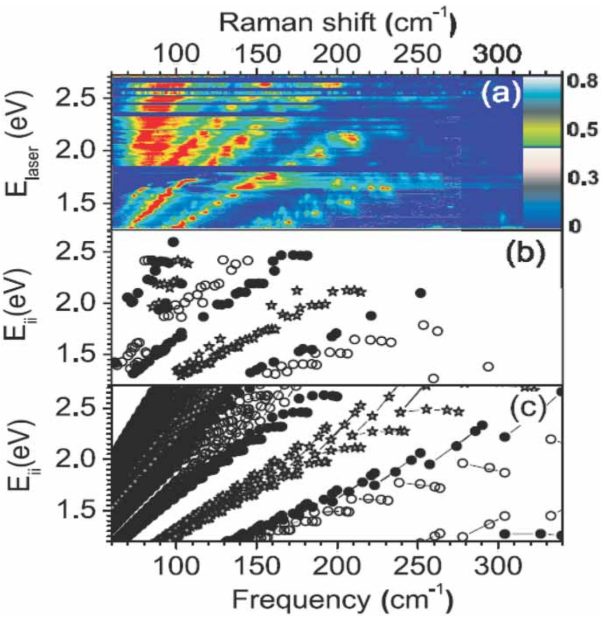

Figure 59. (a) RBM resonance Raman map for the "super-growth" (*S.G.*) SWNT sample [314,335,345]. (b) Kataura plot of all transition energies ($E_{ii}^{S.G.}$) that could be experimentally obtained from the resonance windows extracted from (a) as a function of ω_{RBM}. (c) Kataura plot obtained from Equation (91) with the parameters that best fit the data in (b). The stars stand for M-SWNTs, the open bullets stand for type I S-SWNTs and the filled bullets stand for type II S-SWNTs. Reprinted figure with permission from P.T. Araujo and A. Jorio, Physical Status Solidi B, 2008, 245, pp. 2201–2204 [335]. Copyright © Wiley–VCH Verlag GmbH & Co. KGaA.

general dielectric constant κ on E_{ii}. By "general" we mean that κ comprises the screening from both the tube core electrons and from the tube environment.[24] A d_t-dependent effective κ value for the exciton calculation is needed to reproduce the experimental E_{ii} values consistently. This dependence is important for the physics of quasi -1D and truly 1D materials generally and can be used in interpreting optical experiments and environment effects for such materials. Environmental effects are therefore considered further in Sections 5.2.1 to 5.2.3.

5.2.1. *The effect of the dielectric constant κ on E_{ii}*

Figure 60 shows a map of experimental E_{ii} values (black dots) [314,335] from a SWNT sample grown by the water-assisted ("super-growth") CVD method [34,316]. The resulting data for the E_{ii} transition energies are plotted as a function of the RBM frequencies ω_{RBM}, as obtained by RRS [314,335,345]. In Figure 60, the experimental values of E_{ii} vs. ω_{RBM} for the "super-growth" sample $E_{\text{ii}}^{\text{exp}}$ are compared with the calculated bright exciton energies $E_{\text{ii}}^{\text{cal}}$ (open circles and stars), obtained with the dielectric screening constant $\kappa = 1$. Although $E_{\text{ii}}^{\text{cal}}$ includes SWNT curvature and many-body effects [148], clearly the $E_{\text{ii}}^{\text{exp}}$ values are red shifted when compared with theory, and this red shift depends on both ω_{RBM} (*i.e.*, on d_t) and on the optical energy levels (i in E_{ii}). Figure 63 shows a comparison between the $E_{\text{ii}}^{\text{exp}}$ from the "super-growth" SWNT sample (bullets) [335] and $E_{\text{ii}}^{\text{exp}}$ from the "alcohol-assisted" SWNT sample (open circles) [321]. From Figure 63, we see that besides the changes in ω_{RBM}, the $E_{\text{ii}}^{\text{exp}}$ values from the "alcohol-assisted" SWNTs are generally red shifted with respect to those from the "super-growth" SWNTs. Assuming that κ_{tube} does not change from sample

Downloaded by [Shenzhen University Town] at 19:33 15 August 2011

to sample for a particular type of SWNT sample, since the electronic structure of a given (n,m) tube should be the same, these results indicate that the "alcohol-assisted" SWNTs are surrounded by an environment with a larger κ_{env} value than the "super growth" sample, thus increasing the effective κ and decreasing E_{ii} [229], which is consistent with Figure 61, discussed below.

5.2.2. *Screening effect: a general κ function*

The E_{ii} values can be renormalized in the calculation by explicitly considering the dielectric constant κ in the Coulomb potential energy given by Equation (54) [231]. Here, κ represents the screening of the e–h (e–h) pair by core ($1s$) and σ electrons (κ_{tube}) and by the surrounding materials (κ_{env}), while $\varepsilon(q)$ explicitly gives the polarization function for π-electrons calculated within the RPA [120,148,275]. To fully account for the observed energy-dependent E_{ii} redshift, the total κ values ($1/\kappa = C_{\text{env}}/\kappa_{\text{env}} + C_{\text{tube}}/\kappa_{\text{tube}}$) are fitted to minimize $E_{\text{ii}}^{\text{exp}} - E_{\text{ii}}^{\text{cal}}$ in Figure 60.

The κ values are found to depend on the following three parameters: (1) the subband index p where $p = 1,2,3,4$ and 5 stands for E_{11}^{S}, E_{22}^{S}, E_{11}^{M}, E_{33}^{S} and E_{44}^{S}, respectively [177,229], (2) the diameter of the nanotube d_t and (3) the exciton size l_k in reciprocal space [232]. Using the optimized κ values which are fitted to the calculated E_{ii} values as a function of κ and to the experimental E_{ii} values, a general κ function is modeled to have the following functional form [232]:

$$\kappa \approx C_\kappa \left[p^a \left(\frac{1}{d_t}\right)^b \left(\frac{1}{l_k}\right)^c \right]. \tag{92}$$

The parameters (a,b,c) thus determined are common for all different samples $(a,b,c) = (0.8 \pm 0.1, 1.6 \pm 0.1, 0.4 \pm 0.05)$ so as to both optimize the correlation between κ and (p, d_t, l_k), and to minimize differences between theory and experiment. Here, it should be mentioned that the variable l_k is involved in the κ function because of the screening by the different environments

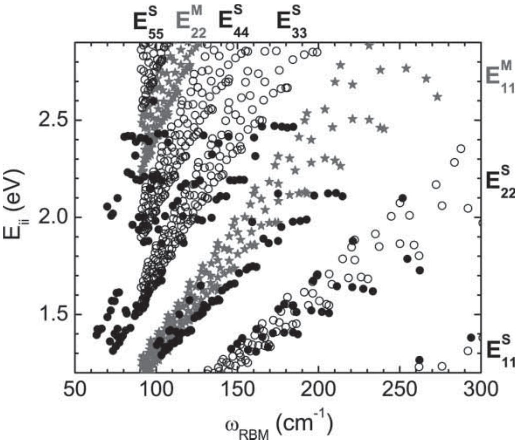

Figure 60. Black dots show $E_{\text{ii}}^{\text{exp}}$ vs. ω_{RBM} results obtained from resonance Raman spectra taken from a super-growth SWNT sample. The black open circles (semiconducting; S-SWNTs) and the dark-gray stars (metallic; M-SWNTs) give $E_{\text{ii}}^{\text{cal}}$ calculated for the bright exciton with a dielectric constant $\kappa = 1$ [148]. Along the x axis, the $E_{\text{ii}}^{\text{cal}}$ values are calculated using the relation $\omega_{\text{RBM}} = 227/d_t$. Due to computer time availability, only E_{ii} for tubes with $d_t < 2.5$ nm (i.e., $\omega_{\text{RBM}} > 91$ cm^{-1}) have been calculated. Transition energies E_{ii}^{S} ($i = 1$ to 5) denote semiconducting SWNTs and E_{ii}^{M} ($i = 1,2$) denote metallic SWNTs. Reprinted figure with permission from P.T. Araujo *et al.*, Physical Review Letters 103, p. 146802, 2009 [229]. Copyright © (2009) by the American Physical Society.

Downloaded by [Shenzhen University Town] at 19:33 15 August 2011

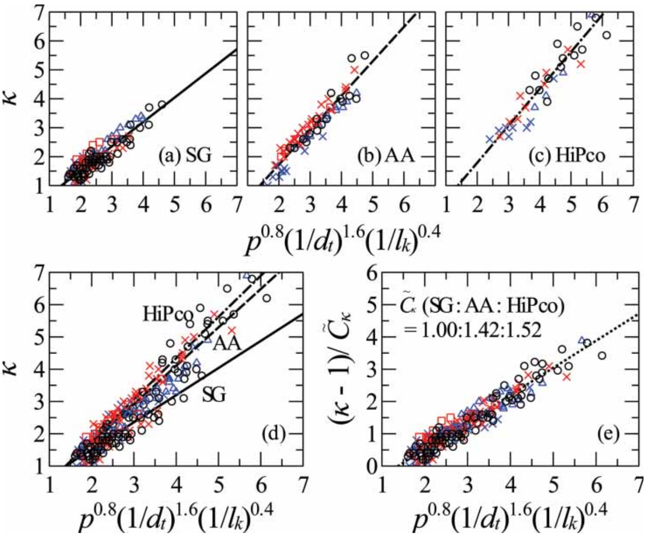

Figure 61. The κ function for: (a) SG, (b) AA, and (c) HiPCO samples. (d) Data for the three different types of samples are plotted on the same figure with a fitted slope C_κ for each sample. (e) All the κ functions collapse on to a single line after dividing each function by the corresponding $\tilde{C}_\kappa$. The following symbols are used: $E_{11}(\circ)$, $E_{22}(\times)$, $E_{33}(\triangle)$ and $E_{44}(\square)$. Black, red, and blue colors, respectively, denote metallic ($\text{mod}(2n+m,3)=0$), semiconductor type I ($\text{mod}(2n+m,3)=1$), and type II ($\text{mod}(2n+m,3)=2$) SWNTs. Reprinted figure with permission from A.R.T. Nugraha *et al.*, Applied Physical Letters 97, p. 91905, 2010 [232]. Copyright © (2010) American Institute of Physics.

which modify the exciton size. However, we will show below that the selection of l_k as a variable for κ is essential for explaining the difference between metallic and semiconducting SWNTs. In fact, Equation (92) indicates another scaling relation for excitons, similar to the previously reported scaling law which relates E_{bd} with d_t, κ, and the "effective mass" μ [275]. However, it is found that the scaling relation involving μ works well only for S-SWNTs and another scaling function is needed for M-SWNTs. This is because E_{bd} for an M-SWNT is screened by free electrons even for a similar effective mass as that for the photo-excited carriers.

In Figure 61, we show a series of results for the κ function [232] for different samples grown by different methods: (a) super-growth [316], (b) alcohol-assisted CVD [347], and (c) the high pressure gas-phase decomposition of CO (HiPCO) [348]. For each sample, the κ function is successfully unified for lower energy transitions ($E_{11}^S, E_{22}^S, E_{11}^M$) and for the higher energy transitions (E_{33}^S, E_{44}^S). Considering l_k explicitly is important for describing the environmental effect for both metallic and semiconducting SWNTs simultaneously, since l_k is very different between metallic and semiconducting SWNTs, even for similar effective mass values because of the screening of the π electrons. When we consider a SWNT, the κ values for the higher E_{ii} transitions which have larger l_k^{-1} values are smaller than those for lower E_{ii} (smaller l_k^{-1}). Thus, l_k^{-1} (the exciton size in real space) is also smaller for the higher E_{ii} because only a small amount of the electric field created by an e–h pair will influence the surrounding materials.[25]

Qualitatively, the origin of the diameter dependence of κ consists of: (1) the diameter-dependent exciton size and (2) the amount of electric field which goes into the surrounding material. These two factors are connected to one another and Ando gave an analytic form for an expression connecting these two factors [349]. The development of an electromagnetic model is needed to fully rationalize Equation (92). Interestingly, the similarity between the κ values found for E_{22}^S and

Downloaded by [Shenzhen University Town] at 19:33 15 August 2011

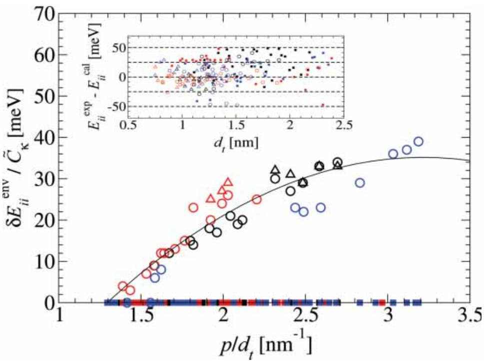

Figure 62. $\delta E_{\text{ii}}^{\text{env}}$ versus d_t, scaled by $\tilde{C}_\kappa$. Circles and triangles, respectively, denote AA and HiPCO samples (see text). Many square symbols on the zero line denote the SG sample which is taken as the standard. The inset shows differences between experimental (exp) and calculated (cal) E_{ii} values for all samples, showing good agreement between experiment and the model calculations. Reprinted figure with permission from A.R.T. Nugraha *et al.*, Applied Physical Letters 97, p. 91905, 2010 [232]. Copyright © (2010) American Institute of Physics.

E_{11}^M shows that the difference between metallic and semiconducting tubes is satisfactorily taken into account by l_k using the random phase approximation (RPA) in calculating $\varepsilon(q)$ [148,342].

In Figure 61(d), three sets of data contained in Figure 61(a)–(c) are merged, from which we know that the three plots when taken together depend only on the difference of the slopes, that is C_κ of Equation (92). Values of C_κ for the SG, AA and HiPCO samples are 0.84, 1.19 and 1.28, respectively. We expect that such differences in the values for C_κ arise from the environmental effects on the exciton energies. Therefore, we assume that each C_κ value characterizes the environmental dielectric constant κ_{env} for that particular sample. The SG sample has the largest E_{ii} and hence the smallest dielectric constant relative to any of the other samples found in the literature [230], and so we normalize C_κ of the SG sample to be $\tilde{C}_\kappa(\text{SG}) = 1.00$ for simplicity. The values of $\tilde{C}_\kappa$ for the other samples can then be determined by taking the ratio of their C_κ values to that for the SG sample. Thus, $\tilde{C}_\kappa$ for the SG, AA, and HiPCO samples becomes 1.00, 1.42, and 1.52, respectively. When we use the normalized $\tilde{C}_\kappa$, all points collapse on to a single line, as shown in Figure 61(e), hence giving justification for the use of this assumption. It is interesting to see that all the lines shown in Figure 61 cross the horizontal axis at $\kappa = 1$ at the same point. This point corresponds to the large diameter limit beyond which the 1D exciton does not exist. The corresponding diameter is scaled by p and l_k.

In Figure 62, we plot the calculated energy shift $\delta E_{\text{ii}}^{\text{env}}$ relative to the SG results as a function of p/d_t. The data on the horizontal axis are the data for the SG sample which should be zero from the definition of $\delta E_{\text{ii}}^{\text{env}}$. The $\delta E_{\text{ii}}^{\text{env}}$ for the AA and HiPCO sample are fitted to a function:

$$\delta E_{\text{ii}}^{\text{env}} = E_{\text{ii}}^{\text{SG}} - E_{\text{ii}}^{\text{env}} \equiv \tilde{C}_\kappa \left[A + B\left(\frac{p}{d_t}\right) + C\left(\frac{p}{d_t}\right)^2 \right], \tag{93}$$

where A, B and C are parameters common to all types of environments and $E_{\text{ii}}^{\text{env}}$ is calculated using the κ function obtained previously. The best fit is found for $A = -42.8\,\text{meV}$, $B = 46.34\,\text{meV}\cdot\text{nm}$ and $C = -7.47\,\text{meV}\cdot\text{nm}^2$. In the inset to Figure 62, we show the energy difference between experiment and theory that is obtained by using the κ function (Equation (92)) and we see all the data points are within 50 meV for a large range of SWNT diameters and energies.

Downloaded by [Shenzhen University Town] at 19:33 15 August 2011

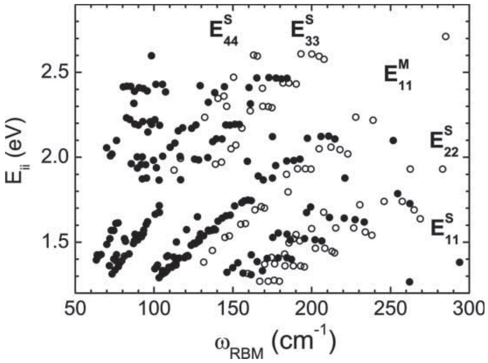

Figure 63. $E^{\rm exp}_{\rm ii}$ vs. $\omega_{\rm RBM}$ results obtained for the "super-growth" (bullets) and the "alcohol-assisted" (open circles) SWNT samples. Reprinted figure with permission from P.T. Araujo *et al.*, Physical Review Letters 103, p. 146802, 2009 [229]. Copyright © (2009) by the American Physical Society.

5.2.3. *Effect of the environmental dielectric constant $\kappa_{\rm env}$ on $E_{\rm ii}$*

Looking at Figure 61, we can observe a difference in the κ values resulting from fitting the $E^{\rm exp}_{\rm ii}$ to the "super-growth" (Figure 61(a)) sample in comparison to the "alcohol-assisted" (Figure 61(b)) SWNT sample. For $E^{\rm S}_{22}$ and $E^{\rm M}_{11}$, we see in Figure 61(a) a clear difference for κ up to $p = 3$ when comparing the two samples. However, for $E^{\rm S}_{33}$ and $E^{\rm S}_{44}$ (Figure 61(d)), no difference in κ in the range $\kappa = 1$–3 can be seen between the two samples. This means that the electric field of the E^S_{33} and E^S_{44} excitons does not extend much outside the SWNT volume, in contrast to the $E^{\rm S}_{22}$ and $E^{\rm M}_{11}$ excitons for which the $\kappa_{\rm env}$ effect is significant. Since the effect of $\kappa_{\rm env}$ is relatively small for energies above $E^{\rm M}_{11}$, it is still possible to assign the (n, m) values from $E^{\rm S}_{33}$ and $E^{\rm S}_{44}$ even if the dielectric constant of the environment is not known, and even though the $E^{\rm S}_{33}$ and $E^{\rm S}_{44}$ values are seen within a large density of dots in the Kataura plot of Figure 63.

5.3. ***Splitting of the G mode***

The first-order Raman-allowed G-band mode in 2D graphene is a single peak feature ($\omega_{\rm G} \approx 1584\,{\rm cm}^{-1}$) [112]. In SWNT, the G-band appears as multiple peaks centered around $\omega_{\rm G}$ [333, 350]. Two, four or six G-band phonons are allowed for the first-order G-band Raman feature in SWNTs, depending on the polarization scattering geometry. Two of these mode, named the totally symmetric A_1 modes (see Figure 64), usually dominate the spectra, although this depends both on the polarization geometry and on the resonance condition. Finally, the G-band profile depends strongly on the metal vs. semiconducting nature of the tube, as well as on changes in the Fermi level. In this section, we discuss the effects responsible for these dependencies, which are related to the effect of curvature and el–ph interaction on the G-band modes.

5.3.1. *The G-band eigenvectors and curvature*

Because of the curvature of the graphene sheet in carbon nanotubes, the longitudinal optical (LO) vs. in-plane transverse optical (iTO) phonons, which are degenerate in graphene, have different frequencies in carbon nanotubes. Actually, the definition of iTO and LO is different for graphene and nanotubes. For 2D systems, transverse and longitudinal are defined with respect to the phonon propagation direction. In the 1D SWNTs, the longitudinal vibration denotes atomic motion along the tube axis, where phonon momentum q can be defined, and the transverse vibration corresponds to atomic motion perpendicular to the tube axis [100,280].

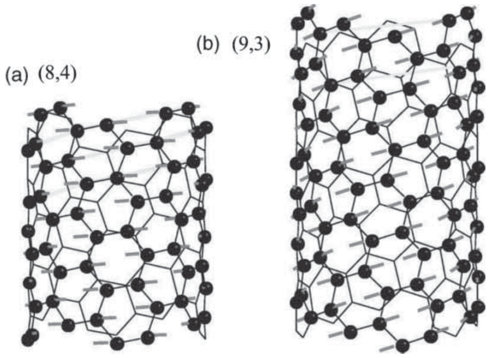

Figure 64. (a) The totally symmetric G-band eigenvectors for the (8,4) semiconducting SWNT. The atomic displacements are almost parallel to the circumference. (b) The totally symmetric G-band eigenvector for the (9,3) metallic SWNT. The atomic displacements are almost parallel to the carbon–carbon bonds. Reprinted figure with permission from S. Reich *et al.*, Physical Review B 64, p. 195416, 2001 [280]. Copyright © (2001) by the American Physical Society.

Downloaded by [Shenzhen University Town] at 19:33 15 August 2011

First-principles calculations have been performed for different SWNTs by Reich *et al.* [280]. They found that, while for armchair and zigzag SWNTs, which have higher symmetry than chiral tube structures, the LO and iTO vibrations of the G-band exist [280], such a definition is not strictly valid for chiral nanotubes, where the atomic vibrations actually depend on the chiral angle. In Figure 64(a and b) Reich *et al.* show the mode displacements for one totally symmetric (A_1) G-band mode in two different chiral SWNTs. For each case, another G-band mode is expected with the atomic vibrations perpendicular to those indicated in the figure. Note that the atomic displacements in Figure 64 are almost perfectly aligned along the circumference in the (8,4) S-SWNT (a), but mostly parallel to the C–C bonds in the (9,3) M-SWNT (b), and in neither case is the strict iTO definition applicable. These findings by Reich *et al.* [280] are qualitatively consistent with other calculations [86], but the quantitative definitions are model-dependent. There is still controversy about whether the many peaks within this G-band can be assigned to LO and iTO type mode behavior, as discussed by Piscanec *et al.* [193].

5.3.2. *The six G-band phonons – confinement effect*

While the doublet nature of the G-band discussed above is related to strain effects from the tube curvature, 1D confinement makes one, two or three of those doublets observable, each pair having either A_1, E_1 or E_2 symmetry. This happens because, when rolling up the graphene sheet to form a nanotube, the zone folding along the circumferential direction generates a larger number of first-order Raman-allowed modes [32,99,100,167].

The difference between A_1, E_1 and E_2 symmetry Raman modes is given by the number of nodes for the atomic motion along the tube circumference, where the number of nodes is zero, two and four, respectively. This zone-folding procedure is shown in Figure 65(b). Therefore, combined with the (quasi) LO and iTO vibrational nature, two, four or six G-band phonons can be Raman-allowed in the Raman spectra from SWNTs, and their observation depends on the polarization of the scattering geometry *and* on the resonance condition, as explained below.

Selecting the Z-axis as the SWNT axis direction, and the Y-axis as the photon propagation direction, light can be polarized parallel (Z) or perpendicular (X) to the nanotube axis. The possible scattering geometries are given by $p_i(\text{is})p_s$, using what is called the Porto notation in memory of S.P.S. Porto, where p_i and p_s give the propagation directions for the incident and scattered

Table 4. Selection rules for polarization dependent G-band features and the corresponding resonance conditions.

Symmetry of phonon	Scattering event	Resonance condition
A_1	(ZZ)	$E_{\text{laser}} = E_{\text{ii}}$, $E_{\text{laser}} \pm E_{\text{G}} = E_{\text{ii}}$
A_1	(XX)	$E_{\text{laser}} = E_{\text{ii}\pm 1}$, $E_{\text{laser}} \pm E_{\text{G}} = E_{\text{ii}\pm 1}$
E_1	(XZ)	$E_{\text{laser}} = E_{\text{ii}\pm 1}$, $E_{\text{laser}} \pm E_{\text{G}} = E_{\text{ii}}$
E_1	(ZX)	$E_{\text{laser}} = E_{\text{ii}}$, $E_{\text{laser}} \pm E_{\text{G}} = E_{\text{ii}\pm 1}$
E_2	(XX)	$E_{\text{laser}} = E_{\text{ii}\pm 1}$, $E_{\text{laser}} \pm E_{\text{G}} = E_{\text{ii}\pm 1}$

The Z- and Y- axes are the SWNT axis direction and the photon propagation direction, respectively. The polarization of the incident and scattered light is given as well as the resonance condition. E_{G} is the G-band phonon energy [1].

Downloaded by [Shenzhen University Town] at 19:33 15 August 2011

photons, respectively, while the incident polarization i and scattered polarization s appear inside the parenthesis (is). Since the SWNT experiments are usually made by using microscopes in the back-scattering configuration, p_{i} and p_{s} are usually Y and $-Y$, so that the simplified notation (is) can be applied. In this case, four different scattering geometries are possible, and these are labeled XX, XZ, ZX and ZZ.

The first-order Raman signal from isolated SWNTs can only be seen when the excitation laser energy is in resonance with a van Hove singularity (VHS) in the JDOS. Chiral SWNTs exhibit C_N symmetry [351,352] and, following the (is) notation introduced above, selection rules imply that: (1) totally symmetric A phonon modes are observed for the (ZZ) scattering geometry when either the incident or the scattered photon is in resonance with E_{ii}, and for the (XX) scattering geometry when either the incident or the scattered photon is in resonance with $E_{\text{i},i\pm 1}$. (2) E_1 symmetry modes can be observed for the (ZX) scattering geometry for resonance of the incident photon with the E_{ii} VHSs, or for resonance of the scattered photon with the $E_{\text{i},i\pm 1}$ VHSs, while for the (XZ) scattering geometry, for resonance of the incident photon with the $E_{\text{i},i\pm 1}$ VHSs, or for resonance of the scattered photon with the E_{ii} VHSs; (3) E_2 symmetry phonon modes can only be observed for the (XX) scattering geometry for resonance with $E_{\text{i},i\pm 1}$ VHSs. Therefore, it is possible to observe two, four or six G-band peaks, depending on the resonance conditions *and* on the polarization scattering geometry, as summarized in Table 4.

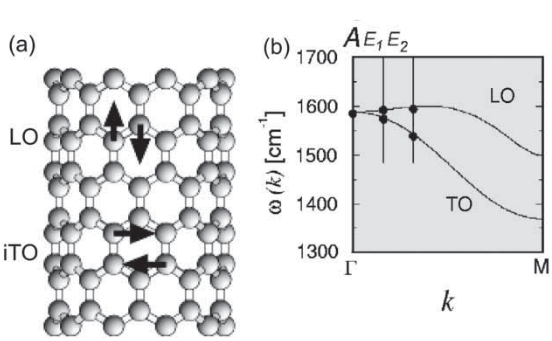

Figure 65. (a) Schematic picture of the G-band atomic vibrations along the nanotube circumference and along the nanotube axis of a zigzag nanotube. (b) The Raman-active modes with A, E_1 and E_2 symmetries and the corresponding cutting lines $\mu = 0$, $\mu = \pm 1$ and $\mu = \pm 2$ in the unfolded 2D BZ. The Γ points of the cutting lines are shown by solid dots. Reprinted from Raman Spectroscopy of Carbon Nanotubes, M.S. Dresselhaus *et al.* [167]. Copyright © (2005) with permission from Elsevier.

Downloaded by [Shenzhen University Town] at 19:33 15 August 2011

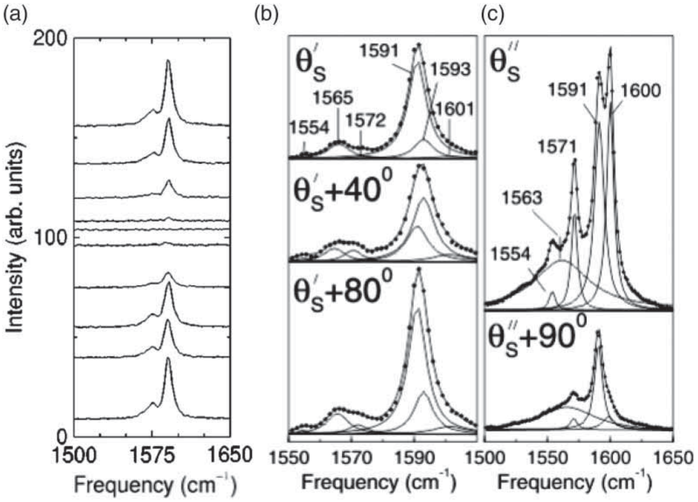

Figure 66. (a) G-band polarization dependence from one isolated semiconducting SWNT sitting on a Si/SiO$_2$ substrate [357]. Both incident and scattered light are polarized parallel to each other and vary from *ZZ* (bottom) to *XX* (middle) and back to *ZZ* (top). (b,c) G-band polarization scattering geometry dependence from two isolated SWNTs. The Lorentzian peak frequencies are given in cm^{-1}. The incident angles θ'_S and θ''_S between the light polarization and the SWNT axis directions are not known *a priori*, but have been assigned as $\theta'_S \sim 0°$ and $\theta''_S \sim 90°$ based on the relative intensities of the polarization behavior of the G-band modes and the expected selection rules and frequencies (see Section 5.3.3) for the A_1, E_1 and E_2 modes [352]. Reprinted figure with permission from A. Jorio *et al.*, Physical Review B 65, p. R121402, 2002 [357]. Copyright © (2009) by the American Physical Society.

Before showing the experimental results related to the selection rules discussed above, we introduce a general polarization behavior that is not accounted for in these selection rules and is responsible for the totally symmetric A$_1$ modes in the G-band spectra which dominate these spectra. Carbon nanotubes are nano-antennas, and both the absorption and emission of light are suppressed when the light is polarized perpendicular to the nanotube axis. This phenomenon is called as the depolarization effect [353,354], where photo-excited carriers screen the electric field of the cross-polarized light inside the carbon nanotube [234,353,354]. Considering these effects, it is clear that the Raman intensity is generally largest for the (ZZ) scattering polarization geometry, while the signal will be suppressed for the (XX) scattering, as shown in Figure 66(a) [355–357]. In addition, remember that the resonance energies are different for light along Z (E_{ii}) and along X $(E_{\mathrm{ii}\pm1})$, as described in Table 4. This means that one rarely observes the Raman signals from parallel (ZZ) and perpendicular $((ZX), (XZ)$ or $(XX))$ polarization directions simultaneously.

Now we can discuss experimental results related to the symmetry selection rules for the different scattering geometries [351,357,358]. Figure 66(b) shows the G-band Raman spectra from a semiconducting SWNT with three different directions for the incident light polarization. Considering θ'_S the initial angle between light polarization and the nanotube axis, unknown *a priori*, the three spectra in Figure 66(b) were acquired with θ'_S, $\theta'_S + 40°$ and $\theta'_S + 80°$. Six well-defined G-band peaks are observed with different relative intensities for the different polarization geometries and, based on the selection rules and on their frequencies (see Section 5.3.3), they are assigned as follows: 1565 and 1591 cm^{-1} are A$_1$ symmetry modes; 1572 and 1593 cm^{-1} are E_1 symmetry modes; and 1554 and 1601 cm^{-1} are E_2 symmetry modes. Figure 66(c) shows the G-band Raman spectra obtained from another semiconducting SWNT, the two spectra with θ''_S and $\theta''_S + 90°$,

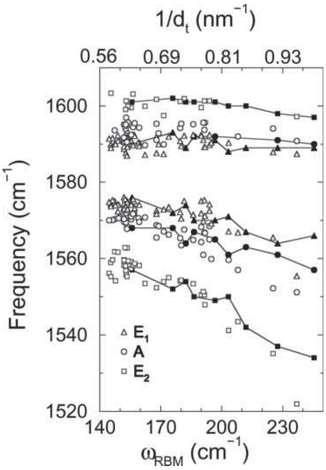

Figure 67. ω_G (open symbols) vs. ω_RBM (bottom axis) and vs. $1/d_t$ (top axis) for S-SWNTs. Explicit experimental G-band data obtained with $E_\mathrm{laser} = 1.58$, 2.41 and 2.54 eV are presented. Solid symbols connected by solid lines give results obtained from *ab initio* calculations [249], downshifted by about 1% to fit the experimental data [352]. Reprinted figure with permission from O. Dubay and G. Kresse, Physical Review B 67, p. 35401, 2003 [249]. Copyright © (2003) by the American Physical Society.

Downloaded by [Shenzhen University Town] at 19:33 15 August 2011

where θ''_S is also unknown *a priori*. The spectra requires four sharp Lorentzians for a good lineshape fitting, plus a broad feature at about 1563 cm^{-1}. This broad feature (FWHM $\sim$ 50 cm^{-1}) is sometimes observed in weakly resonant G-band spectra from SWNTs, and is generated by defect-induced DR processes. For the sharp peaks, based on the polarization Raman studies and on their relative frequencies [351], the 1554 and 1600 cm^{-1} peaks are E_2 symmetry modes, while the 1571 and 1591 cm^{-1} peaks are unresolved $(\mathrm{A}_1 + \mathrm{E}_1)$ symmetry modes, with their relative intensities depending on the incident light polarization direction [351].

Generally speaking, the intensity ratio between the two scattering geometries $ZZ : XX$ can assume values either larger or smaller than 1, depending on the resonance condition. Observation of the spectra with (XX) polarization in Figure 66(c) indicates resonance with a $E_{\mathrm{i},i\pm1}$ optical transition. In samples with a large diameter distribution, e.g. d_t from 1.3 nm up to 2.5 nm in Ref. [351], both the E_ii and $E_{\mathrm{i},i\pm1}$ transitions can occur within the resonance window of the same laser, and an average value of $\mathrm{ZZ} : \mathrm{XX} = 1.00 : 0.25$ was then observed. However, for most isolated SWNTs, the Raman intensities exhibit an intensity ratio $I_{ZZ} : I_{XX} \sim 1 : 0$. This "antenna effect" is observed for samples in resonance with only E_ii electronic transitions, as shown in [355–357].

Finally, the above discussion is related to phonon confinement within the first-order *single resonance* process [333,350,351]. There has been interesting discussion on whether the features in the multi-peak G-band could all be assigned to A_1 symmetry modes [355,359] originating from a defect-induced DR Raman scattering process [145]. It seems that both cases, i.e. a multi-peak feature from multi-symmetry scattering and from an A_1 symmetry feature induced by disorder are possible in very disordered samples [360].

5.3.3. *The diameter dependence of the G band phonon frequencies*

The G-band mode assignment proposed in Section 5.3.2 comes from a comparison between experimental results and *ab initio* calculations of the diameter dependence of ω_G [249], as shown

Downloaded by [Shenzhen University Town] at 19:33 15 August 2011

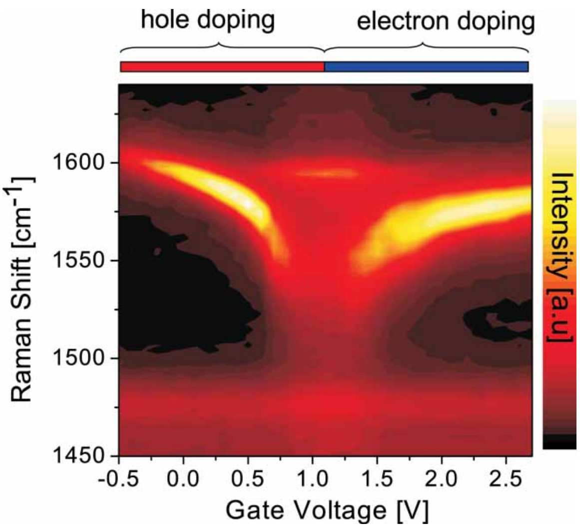

Figure 68. Experimental intensity plot of the G-band spectrum of a metallic SWNT as a function of electrochemical gate potential. For this nanotube the charge neutrality point, corresponding to the Dirac point, is 1.2 V. Adapted figure with permission from M. Farhat *et al.*, Physical Review Letters 99, p. 145506, 2009 [201]. Copyright © (2009) by the American Physical Society.

in Figure 67. The relation between ω_{RBM} (bottom axis – for experimental results) and inverse nanotube diameter (top axis – for theoretical results) were made in this figure considering $1/d_t = \omega_{\mathrm{RBM}}/248$. This $\omega_{\mathrm{RBM}} = 248/d_t$ relation [111] was broadly used in the early years of single nanotube spectroscopy (2001–2005). The present understanding uses Equation (86) with $C_e = 0.065$, which is applicable to a larger variety of samples.

The spectra in this work were fit using 2, 4 or 6 peaks with FWHM $\gamma_{\mathrm{G}} \sim 5\,\mathrm{cm}^{-1}$, which is the natural linewidth for the G-band modes [340]. The diameter dependent downshift in frequency comes from strain and from curvature-induced mixing of low frequency out-of-plane components. In the time-independent perturbation picture, the $\omega_{\mathrm{G}}^{\mathrm{LO}}$ mode frequency is expected to be independent of diameter, since the atomic vibrations are along the tube axis. In contrast, the $\omega_{\mathrm{G}}^{\mathrm{TO}}$ mode has atomic vibrations along the tube circumference, and increasing the curvature increases the out-of-plane component, thus decreasing the spring constant with a $1/d_t^2$ dependence. This picture holds for semiconducting SWNTs, where G^+ now stands for the LO mode, and G^- stands for the iTO mode [171]. However, for metallic SWNTs the picture is different: G^+ now stands for the iTO mode, and G^- stands for the LO mode [193,249]. The G-band profile in this case is very different and depends strongly on doping, as shown in Figure 68, and this behavior can only be understood within a time-dependent perturbation picture. In this section, we focus on the spectra from semiconducting SWNTs. Metallic SWNTs are discussed in Section 5.4.

The d_t dependence of the frequencies for each of the three higher frequency G^+ band modes (A_1, E_1 and E_2) observed experimentally are in very good agreement with theory [249], showing basically no diameter dependence. For the lower frequency G^- band modes, both *ab initio* calculations and the experimental results show a considerable d_t dependence of the mode frequency. The experimental G-band frequencies from semiconducting SWNTs can be fit with [352]

$$\omega_{\mathrm{G}} = 1592 - \frac{C}{d_t^{\beta}}, \tag{94}$$

where the values for the various parameters are: $\beta = 1.4$, $C_{A_1} = 41.4\,\mathrm{cm}^{-1}\,\mathrm{nm}$, $C_{E_1} = 32.6\,\mathrm{cm}^{-1}\,\mathrm{nm}$ and $C_{E_2} = 64.6\,\mathrm{cm}^{-1}\,\mathrm{nm}$.

A simpler formula for the G-band intensities has also been proposed in Ref. [171], where the G-band fitting is not performed with six Lorentzians, but rather by considering just the peak value for the two most intense features. In this case, the higher frequency G^+ peak is diameter independent and the lower frequency G^- feature decreases in frequency with a $1/d_t^2$ dependence. In practice, the G band can be used for a diameter determination for both semiconducting and metallic SWNTs by using the formula from [171]. For more detailed studies, the more complete analysis discussed above and including dynamic effects [193] and environmental effects [232] should be used.

Downloaded by [Shenzhen University Town] at 19:33 15 August 2011

5.4. *Kohn Anomaly effect on the G-band and the RBM mode*

In this section, the first-order spectra for metallic SWNTs are discussed giving special attention to the dependence of these spectral features on the Fermi level position and the KA phenomena that account for the special properties of these spectral features for metallic SWNTs [193]. First, we discuss the characteristics of the KA for the G-band in Section 5.4.1 through Section 5.4.4, followed by an elaboration of the KA for the RBM feature in Section 5.4.5.

5.4.1. *G-band Kohn anomaly*

The Fermi-level dependencies of the LO and iTO modes on SWNT bundles have been measured [50,51,361,362], showing mainly changes in frequency and linewidth of the Breit–Wigner–Fano (BWF)-like feature in the G-band associated with metallic nanotubes, as E_F was varied. This effect is now understood within the framework of time-dependent perturbation theory including dynamic effects [193], and this effect has been shown more clearly with Fermi level variation experiments performed on individual metallic carbon nanotubes [193,201,283]. The G-band spectrum of an individual metallic nanotube changes as a function of an electrochemical gate potential as shown in Figure 68. The higher frequency peak does not change significantly as a function of gate voltage, but the broad lower frequency peak (BWF-like) upshifts and narrows in linewidth with both positive and negative changes in the Fermi level. Differently from semiconducting SWNTs, where the higher frequency peak is assigned to the LO vibration, metallic SWNTs have a lower frequency mode with a BWF-like lineshape that is assigned to the LO mode, which downshifts in energy significantly due to the KA effect [193].

The KA is predicted to occur in metallic carbon nanotubes [193], and to exhibit two characteristic signatures related to non-adiabatic effects: (1) within the energy window $E_\mathrm{F} < |\hbar\omega_\mathrm{LO}|$, the LO phonon peak is broadened due to the creation of real e–h pairs; (2) the LO frequency vs. E_F curve shows a characteristic “W” lineshape due to the two singularities located at $E_\mathrm{F} = \pm\hbar\omega_\mathrm{LO}$. This “W” lineshape is not resolved in Figure 68 because of inhomogeneous charging due to trapped charges on the substrate that result in a smearing of E_F. However, using pristine suspended nanotubes that are gated electrostatically, the “W” feature can be explicitly seen in the frequency dependence of the LO mode [363].

The intensities of the LO and iTO modes depend also on the chiral angle, with the iTO mode being symmetry forbidden for a zigzag nanotube [283,364]. A chiral angle dependence of the iTO mode softening has been predicted theoretically [365]. Future experiments on structurally identified and truly isolated individual (n, m) nanotubes are needed to further advance our understanding of these phenomena related to the KA.

Gate-dependent experiments on semiconducting nanotubes reveal that their G-band phonons also experience energy renormalization due to el–ph coupling [51,366]. However, $\hbar\omega_\mathrm{LO/iTO} < E_{11}^S$

Downloaded by [Shenzhen University Town] at 19:33 15 August 2011

for semiconducting SWNTs, which means that the G-band phonons are unable to create real e–h excitations across a typical non-zero bandgap. Therefore, lifetime broadening of the phonon is not expected, and the G-band peak FWHM should not change significantly. Still, virtual e–h excitations contribute to the softening of the phonon energies [366]. Both the iTO and LO modes couple to intermediate e–h pairs, and the iTO mode is expected to show a greater E_F-dependent frequency shift, most significantly in larger diameter nanotubes, as the band gap energy approaches the phonon energy [366]. This behavior in semiconducting SWNTs is opposite to metallic SWNTs.

5.4.2. *Chemical doping and the G band*

The KA effect discussed in Section 5.4.1 is important at low doping levels. For higher doping levels, structural distortions dominate, and these distortions depend on the level of the *p* vs. *n* doping, which should cause upshift vs. downshift in the phonon frequencies, respectively. Such *p* vs. *n* doping behavior has been demonstrated for the G band of single-wall and multi-wall carbon nanotubes doped chemically with atomic species that are donors or acceptors to carbon [36,367]. For example, the doping with K, Rb and Cs (alkali metals) leads to a G-band mode softening of $35\,\mathrm{cm}^{-1}$ accompanied by significant changes in the G-band lineshape. For SWNT bundles doped with Br_2 (halogens), an upshift in the Raman-mode frequencies is observed. For more details on the effect of chemical doping on the Raman spectra of SWNTs, see, e.g. [36].

5.4.3. *Substrate interaction and the G band*

The confocal image shown in Figure 69(a) was obtained by integrating the G-band Raman signal from a SWNT serpentine sample, while raster scanning the sample [324]. These carbon serpentine nanotubes are SWNTs with parallel straight segments connected by alternating U-turns, as shown in Figure 69(a) [324]. These serpentine nanotubes were grown by catalytic CVD on miscut single-crystal quartz wafers [368]. The resulting vicinial SiO_2 (1 1 0 1) substrate is insulating, and is terminated by parallel atomic steps. At the temperature of nanotube growth, the surface contains exposed unpassivated Si atoms, thus enabling a strong tube–substrate interaction to occur, especially when the nanotube lies along a step. Alternatively, when the nanotube lies across the surface steps, the interaction is discontinuous and weaker. The orientation between the tube and crystalline quartz varies, which means that the tube–substrate interaction is modulated along the tube. The straight segments usually lie along the quartz steps, while the U-turns lie across the steps. Figure 69(b) shows the G-band Raman spectra obtained from all 41 points indicated by the pointers in Figure 69(a). Careful analysis of the individual G-band spectral features shows that the G-band spectra changes along the SWNT serpentine. These changes are related to strain and doping which varies along the tube due to the morphology of the tube–substrate interaction in these samples [324]. Such a strong interaction also has a strong effect on the RBM frequencies, leading to an environmental constant of $C_e = 0.085$ in Equation (86) which relates ω_{RBM} and d_t [323].

5.4.4. *Theoretical approach to the Kohn Anomaly*

The KA in metallic SWNTs was introduced firstly by Piscanec *et al.* [193]. As discussed in Section 3.6.5, the phonon softening phenomena is understood by second-order perturbation theory in which a phonon virtually excites an e–h pair across the metallic energy subband of a metallic SWNT (as shown in Figure 70(a)). The effective Hamiltonian in second-order perturbation theory is given by Equation (71) [196,205,246]. In Figure 70(b), we show the energy denominator of Equation (71), in which the real part of $h(E)$ is related to the frequency shift, while the imaginary part of $h(E)$ is related to the spectral broadening. From this figure, for the energy below (above) the phonon energy of the G-band, the virtual excitation contributes to the phonon hardening

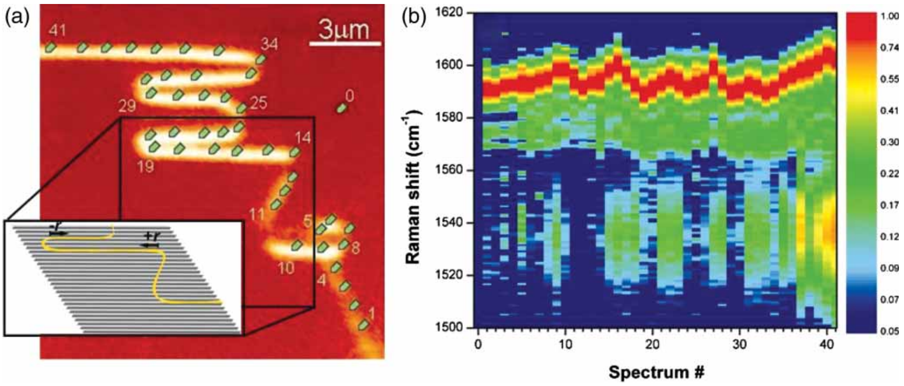

Figure 69. (a) Confocal image of the G-band integrated intensity using a laser wavelength $\lambda_{\text{laser}} = 632.8\,\text{nm}$ ($E_{\text{laser}} = 1.96\,\text{eV}$). The inset shows a schematic view of the SWNT (yellow) lying on top of the miscut quartz. (b) The G-band Raman spectra obtained at the 41 points indicated and numbered in (a). There is a modulation of the higher frequency G^+ feature ($\sim$1590-1605 cm^{-1}) along with the appearance and disappearance of the lower frequency G^- feature ($\sim$1540 cm^{-1}). This appearance and disappearance of the G^+ and G^- features are related to the tube-substrate morphology and interaction. Adapted with permission from J.S. Soares *et al.*, Nono Letters 10, pp. 5043–5048, 2010 [324]. Copyright © (2010) American Chemical Society.

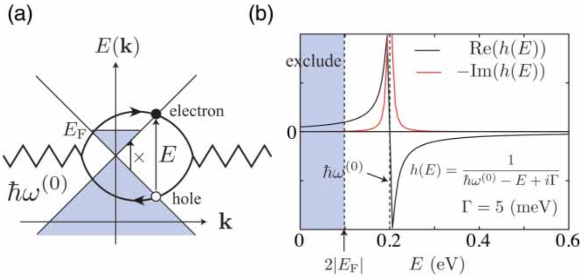

Figure 70. (a) An intermediate e–h pair state that contributes to the energy shift of the optical phonon modes is depicted. A phonon mode is denoted by a zigzag line and an e–h pair is represented by a loop. The low energy e–h pair satisfying $0 \leq E \leq 2|E_F|$ is forbidden at zero temperature by the Pauli principle. (b) The energy correction to the phonon energy by an intermediate e–h pair state, especially the sign of the correction, depends on the energy of the intermediate state as $h(E)$. Adapted figure with permission from K. Sasaki *et al.*, Physical Review B 78, pp. 235405–235411, 2008 [365]. Copyright © (2008) by the American Physical Society.

(softening). Thus, when the phonon hardening processes are suppressed by increasing the Fermi energy, we get a large phonon softening and broadening at $2E_F = \pm 0.2\,\text{eV}$. This is the origin of the observed W lineshape [196]. Recent measurements of the G-band spectra at $T = 12\,\text{K}$ show phonon anomalies at $E_F = \pm\hbar\omega_G/2$ that could be clearly distinguished experimentally [200]. Furthermore, the el–ph matrix element for this virtual excitation has a chiral angle dependence that acts differently for iTO and LO phonons [196]. For example, the el–ph interaction for the iTO phonon is absent (no KA effect) for armchair nanotube, while phonon hardening of the iTO mode occurs for zigzag nanotubes. Thus, a detailed analysis of the LO and iTO phonon modes as a function of the Fermi energy gives important information about the (n, m) assignment for metallic carbon nanotubes. For a detailed description of these phenomena, see [193,196,205,246].

Downloaded by [Shenzhen University Town] at 19:33 15 August 2011

Downloaded by [Shenzhen University Town] at 19:33 15 August 2011

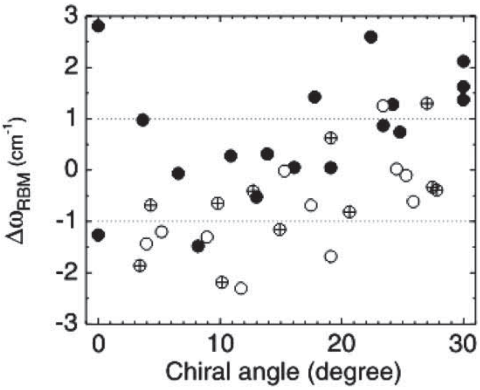

Figure 71. Deviation of the experimentally observed RBM frequency (ω_{RBM}) from the linear dependence given by $(218.3/d_t + 15.9)$, as a function of θ for a particular HiPCO nanotube sample. Filled, open and crossed circles denote M-SWNTs, type I and type II S-SWNTs, respectively. The dotted lines show an experimental accuracy of $\pm 1\,\text{cm}^{-1}$. Reprinted figure with permission from A. Jorio *et al*., Physical Review B 71, p. 75401, 2005 [369]. Copyright © (2005) by the American Physical Society.

5.4.5. *RBM band and G-band Kohn anomaly*

The diameter dependence of the RBM frequency ω_{RBM} can be described by elasticity theory, as presented in Section 5.1.1. However, there are two effects that are not considered by elasticity theory when discussing the ω_{RBM}, the first related to the chirality-dependent distortion of the lattice, and the second related to the el–ph coupling occurring in metallic SWNTs. The first effect should be observable in SWNTs with $d_t \lesssim 1\,\text{nm}$ SWNTs, where the curvature-induced lattice distortion is important, while the second should be observable in metallic SWNTs.

Figure 71 shows a plot of the deviations of the observed ω_{RBM} values from the best linear $1/d_t$ dependence that fits all the experimental data $[\Delta\omega_{\text{RBM}} = \omega_{\text{RBM}} - (218.3/d_t + 15.9)]$ as a function of chiral angle θ, for SWNTs grown by the HiPCO (high pressure CO CVD) method [369]. Deviations of the points from $\Delta\omega_{\text{RBM}} = 0$ are clearly seen, with interesting trends in the deviations: (i) metallic SWNTs (solid bullets) exhibit systematically larger $\Delta\omega_{\text{RBM}}$ when compared with semiconducting SWNTs (open bullets); (ii) $\Delta\omega_{\text{RBM}}$ depends on the chiral angle θ, showing an increase in $\Delta\omega_{\text{RBM}}$ with increasing θ from zigzag (0°) to armchair (30°) SWNTs.

Because of tube curvature, there is sp^2–sp^3 mixing, and the RBM frequencies decrease with respect to their ideal values as the SWNT diameter decreases [254,370]. In armchair tubes, the circumferential strain is more evenly distributed between the bonds, leading to smaller bond elongations. This is a purely geometric effect, related to the directions of the three C–C bonds with respect to the circumferential direction. Since the RBM softening is directly related to the bond elongation along the nanotube circumference, a larger softening of ω_{RBM} for zigzag tubes relative to armchair tubes is expected, as is shown in Figure 71 [369].

Finally, similar to the effect discussed for the G-band, a phonon frequency shift of the RBM for metallic SWNTs was predicted [193,365] and observed experimentally [204] as a function of the Fermi energy, although a much smaller shift ($\sim 3\,\text{cm}^{-1}$) due to the KA effect is expected for ω_{RBM} than for ω_{G}. Furthermore, in the chiral and zigzag metallic SWNTs, a mini-gap exists and, when the gap is larger than $\hbar\omega_{\text{RBM}}$, then the KA effect disappears. There is a lower limit of d_t (1–1.8 nm depending on chiral angle) below which the KA effect for the RBM phonon cannot be observed, since the mini-gap is proportional to $1/d_t^2$ and $\hbar\omega_{\text{RBM}}$ is proportional to $1/d_t$ [365].

Downloaded by [Shenzhen University Town] at 19:33 15 August 2011

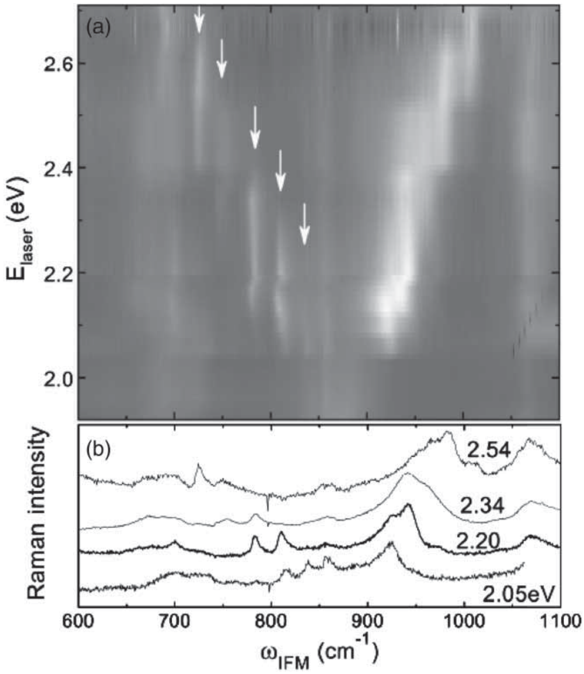

Figure 72. (a) 2D plot of the E_{laser} dependence for the Raman spectra of SWNT bundles in the intermediate frequency mode (IFM) range. The bright, light areas indicate high Raman scattering intensity. Arrows point to five well-defined ω_{IFM} features. (b) Raman spectra in the corresponding IFM range are taken at discrete laser excitation energies $E_{\text{laser}} = 2.05, 2.20, 2.34$, and 2.54 eV. Reprinted figure with permission from C. Fatini *et al.*, Physical Review Letters 93, p. 87401, 2005 [371]. Copyright © (2003) by the American Physical Society.

5.5. *Double resonance effect and quantum confinement*

Like in graphene, SWNTs exhibit dispersive bands related to the DR effect. However, for SWNTs the Raman signal is dominated by resonance effects associated with van Hove singularities. The vertical stripes in Figure 72(a) define the resonance window for a given resonance band, for a given (n, m) SWNT within a SWNT-bundle sample. The modes appearing in the spectral region between 400 and 1200 cm^{-1} have been named intermediate frequency modes (IFMs), making reference to their frequencies being between the commonly studied RBM and G modes. The IFM features are related to combinations of out-of-plane transverse modes (oTO) and longitudinal acoustic modes (LA), more specifically oTO ± LA [371,372] in the 2D-unfolded graphene system. Up to now, it is not yet clear whether or not these modes are activated by defects. Theory relates the observation of the IFMs to quantum confinement effects along the tube length [373], and some experimental evidence has been found to support such theory [374].

The G′ peak [193,310,375] in the Raman spectra for SWNTs, shows a dispersive behavior with laser excitation energy, but some unique characteristics are observed due to the 1D structure of SWNTs. We will detail these results in the next two sections, where in Section 5.5.1 we show the G′ behavior for SWNT bundles, and in Section 5.5.2 we discuss the G′-band behaviour in isolated SWNTs.

Downloaded by [Shenzhen University Town] at 19:33 15 August 2011

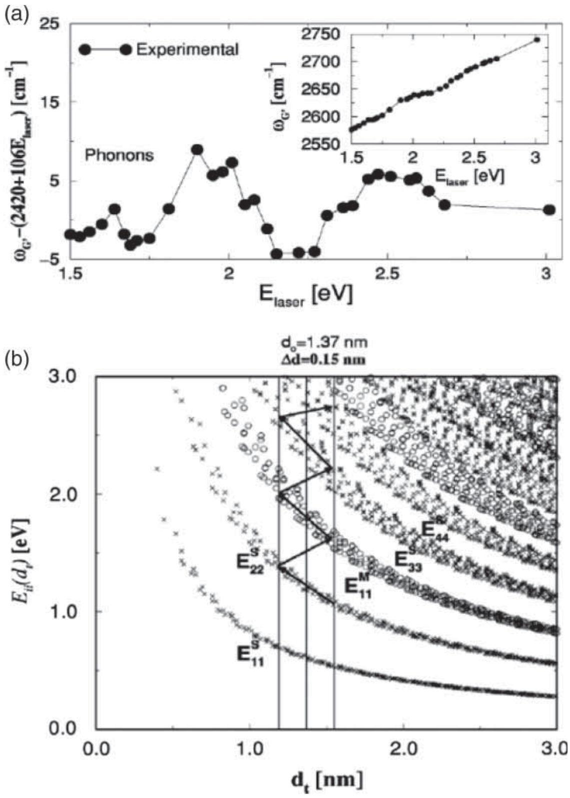

Figure 73. (a) G′-band data for $\omega_{G'}$ for a SWNT bundle sample taken from [222] after subtracting the linear dispersion $2420 + 1106E_{\text{laser}}$ from the $\omega_{G'}$ vs. E_{laser} data shown in the inset. (b) Optical transition energies E_{ii} as a function of diameter for SWNTs. The vertical lines denote the diameter range of the SWNT bundle used in the G′-band dispersion experiment shown in (a). Reprinted figure with permission from A.G. Souza Filho *et al.*, Physical Review B 65, p. 35404, 2001 [376]. Copyright © (2001) by the American Physical Society.

5.5.1. *The G′-band in SWNT bundles*

For SWNT bundles, most of the (n, m) dependent 1D-related effects are averaged out, and a close relation is observed experimentally between the G′-band in SWNTs and in graphene. However, anomalous effects are still observed, and these effects are related to the 1D structure of the material in the nanotube bundle. The inset to Figure 73(a) shows the dispersion of the $\omega_{G'}$ frequency in cm^{-1} in SWNT bundles. Fitting the observed linear dispersion of $\omega_{G'}$ for SWNTs [222] gives

$$\omega_{G'} = 2040 + 106E_{\text{laser}}, \tag{95}$$

which is consistent with observations in graphene and graphite. However, different from graphene and graphite, the G′-band dispersion in SWNTs exhibits a superimposed oscillatory behavior as a function of E_{laser}, as shown in Figure 73(a), where the linear dispersion effect was subtracted from the experimentally observed frequencies. The oscillatory behavior seen in Figure 73(a) is due to the $\omega_{G'}$ dependence on tube diameter, as discussed below.

The G′-band frequency ($\omega_{G'}$) depends on tube diameter (d_t) because of a force constant softening, which is associated with the curvature of the nanotube wall. Experiments on isolated tubes

Downloaded by [Shenzhen University Town] at 19:33 15 August 2011

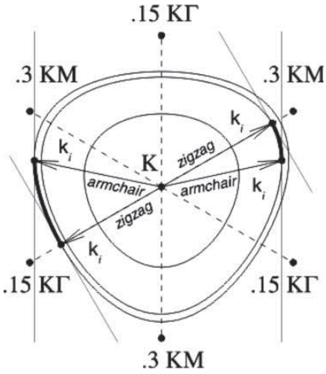

Figure 74. Cutting lines for two metallic SWNTs, one zigzag and one armchair, in the unfolded 2D BZ of graphene. The wavevectors k_{i} point with arrows to the locations where the van Hove singularities occur. Reprinted figure with permission from G.G. Samsonidze *et al.*, Physical Review Letters 90, p. 27403, 2003 [378]. Copyright © (2003) by the American Physical Society.

show that [377]

$$\omega_{\mathrm{G}'} = \omega_{\mathrm{G}'_0} - \frac{35.4}{d_t}, \tag{96}$$

where $\omega_{\mathrm{G}'_0}$ is the laser energy-dependent value observed in graphene, which can be considered to be the limiting value of $\omega_{\mathrm{G}'}$ for an infinite diameter tube. This diameter dependence of $\omega_{\mathrm{G}'}$ is the critical factor behind the oscillatory behavior observed in Figure 73(a). The vertical lines in Figure 73(b) denote the diameter range of the SWNTs contained in the SWNT bundle used in the G′-band dispersion experiment illustrated in Figure 73. When moving along an arrow by increasing the excitation laser energy, for example, within the E_{22}^S subband by changing the E_{laser}, value, just above 1 eV, different SWNTs with different diameters enter and leave the resonance window for a given E_{ii} optical transition. By increasing the laser energy, the diameters of the tubes that are in resonance decrease, thus increasing the expected energy due to the DR process. When the resonance condition with E_{laser} jumps from one interband transition to another, e.g., from E_{22}^S to E_{11}^M, which occurs at around $E_{\mathrm{laser}} = 1.5$ eV, the nanotube diameter jumps to higher values. This process modulates the $\omega_{\mathrm{G}'}$ dispersion, as observed by the oscillatory behavior shown in Figure 73(a).

The “continuous” frequency dispersion observed in Figure 73(b) is a result observed in SWNT bundles where different tubes enter and leave resonance, thus probing the whole unfolded 2D BZ. This result is clearer for the IFMs as shown in Figure 72. The 1D confinement effects on the G′ spectra can only be clearly seen in experiments at the individual isolated SWNT level, discussed further in Section 5.5.2.

5.5.2. *The* (n, m) *dependence of the G′-band; phonon trigonal warping*

This section gives an appreciation of the effect of 1D confinement on the G′ feature in SWNTs at the individual SWNT level. In the case of SWNTs, the resonance condition is restricted to $E_{\mathrm{laser}} \approx E_{\mathrm{ii}}, E_{\mathrm{ii}} \pm E_{\mathrm{ph}}$ (the resonant transition energy between van Hove singular energies). This fact gives rise to a $\omega_{\mathrm{G}'}$ dependence on the SWNT diameter (see Section 5.5.1) *and* on the chiral angle.

Figure 74 shows the cutting lines for two metallic SWNTs, one zigzag and one armchair, in the unfolded 2D BZ of graphene. The van Hove singularities occur where a cutting line is tangent to

Downloaded by [Shenzhen University Town] at 19:33 15 August 2011

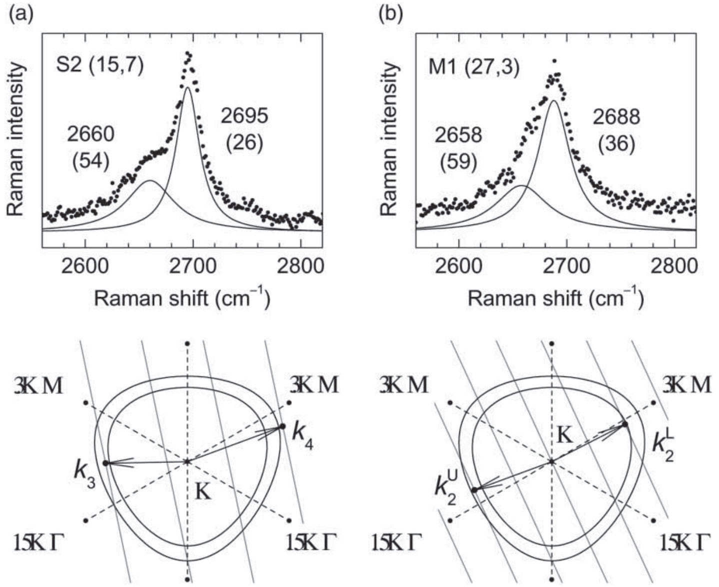

Figure 75. The G′-band Raman spectra for (a) a semiconducting $(15, 7)$ and (b) a metallic $(27, 3)$ SWNT, showing two-peak structures [375,378,379], respectively. The *vicinity* of the K point in the unfolded BZ is shown in the lower part of the figure, where the equi-energy contours for the incident $E_{\text{laser}} = 2.41$ eV and the scattered $E_{\text{laser}} - E_{\text{G}'} = 2.08$ eV photons, together with the cutting lines and wave vectors for the resonant van Hove singularities ($E_{33}^{S} = 2.19$ eV, $E_{44}^{S} = 2.51$ eV, $E_{22}^{M(\text{L})} = 2.04$ eV, $E_{22}^{M(\text{U})} = 2.31$ eV) are shown. Reprinted figures from A.G. Souza Filho *et al.*, Physical Review B 65, p. 85417, 2002 [375]. Copyright © (2002) by the American Physical Society and A.G. Souza Filho *et al.*, Chemical Physics Letters 354, pp. 62–68, Copyright © (2002) with permission from Elsevier.

an equi-energy contour, thus causing a chiral angle dependence on the k_{i} value where a particular excited state k_{i} occurs. The states at k_{i} are those responsible for the dominant optical spectra observed in SWNTs, including the DR features. The presence of cutting lines in carbon nanotubes is expected to affect all the dispersive Raman features [376], but here we focus on the G′-band, because the G′-band dispersion is very large and is an interesting effect.

The two-peak G′-band Raman features in the Raman spectra observed from semiconducting and metallic isolated nanotubes are shown in Figure 75(a) and (b), respectively. The presence of two peaks in the G′-band Raman feature indicates the resonance with both the incident E_{laser} and scattered E_{laser}–$E_{\text{G}'}$ photons, respectively, with two different van Hove singularities (VHSs) for the same nanotube. E_{laser} and E_{laser}–$E_{\text{G}'}$ are defined in Figure 75(a) and (b) below the G′-band spectra, by the outer and inner equi-energy contours near the 2D BZ boundary, in which the cutting lines are shown and the trigonal warping of these constant energy contours can be seen [380]. The two peaks in Figure 75(a) and (b) can be associated with the phonon modes of the wave vectors $\vec{q}_i = -2\vec{k}_{\text{i}}$, where $i = 3, 4, 2\text{L}, 2\text{U}$ relate to $E_{33}^{S}, E_{44}^{S}, E_{22}^{\text{ML}}$ and E_{22}^{MU}, respectively, and the electronic wave vectors $\vec{k}_{\text{i}}$ are shown in the lower part of Figure 75. For the semiconducting SWNT shown in Figure 75(a), the resonant wave vectors $\vec{k}_3$ and $\vec{k}_4$ have different magnitudes, $k_4 - k_3 \simeq K_1/3$, resulting in twice the difference for the phonon wave vectors, $q_4 - q_3 \simeq 2K_1/3 = 4d_t/3$, so that the splitting of the G′-band Raman feature arises from the *phonon dispersion* $\omega_{\text{ph}}(q)$ around the K point. In contrast, for the metallic nanotube (M-SWNT) shown in Figure 75(b), the resonant wave vectors $\vec{k}_2^{\text{L}}$ and $\vec{k}_2^{\text{U}}$ have roughly equal magnitudes and opposite directions away from the K

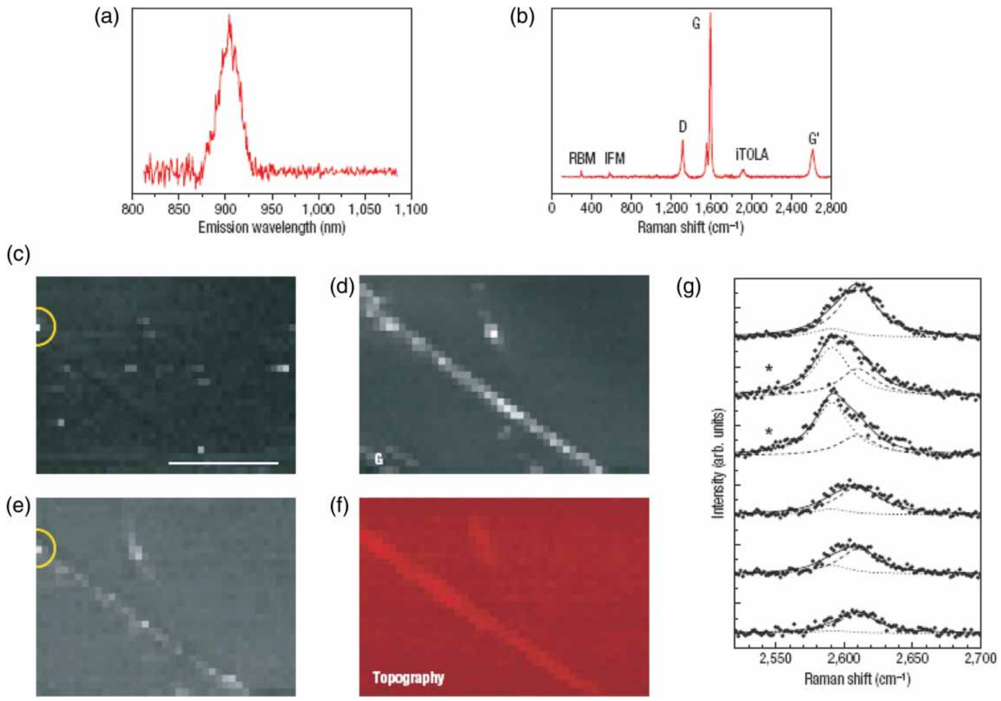

Figure 76. Localized excitonic emission in a semiconducting SWNT. (a) Photoluminescence emission at $\lambda_{\rm em} = 900$ nm from a single SWNT. (b) Raman spectrum recorded from the same SWNT. The spectral position of the RBM, $\omega_{\rm RBM} = 302\,{\rm cm}^{-1}$, together with the $\lambda_{\rm em} = 900$ nm information, leads to the (9,1) assignment for this tube. (c) Near-field photoluminescence image of the SWNT revealing localized excitonic emission. (d)–(e) Near-field Raman imaging of the same SWNT, where the image contrast is provided by spectral integration over the G and D bands, respectively. (f) Corresponding topography image. The circles indicate localized photoluminescence (c) and defect-induced (D band) Raman scattering (e). The scale bar in (c) denotes 250 nm. (g) Evolution of the G′-band spectra near the defective segment of the (9,1) SWNT. The spectra were taken in steps of 25 nm along the nanotube, showing the defect-induced G′ peak (dotted Lorentzian). The asterisks denote the spatial locations where localized photoluminescence and defect-induced D-band Raman scattering were measured (see circles in (c) and (e), respectively). Reprinted with permission from I.O. Maciel *et al.*, Nature Materials 7, pp. 878–883, 2008 [293]. Copyright © (2008) American Institute of Physics.

Downloaded by [Shenzhen University Town] at 19:33 15 August 2011

point, so that the splitting of the G′-band Raman feature for metallic nanotubes arises from the *anisotropy* of the phonon dispersion $\omega_{\rm ph}(q)$ around the K point [378], which we identify with the phonon trigonal warping effect. Overall, the presence of two peaks in the DR Raman features of isolated carbon nanotubes is associated with quantum confinement effects expressed in terms of cutting lines.

Of course the G′-band is not the only feature to exhibit an (n,m) dependence for SWNT systems. Actually, all the DR features are expected to exhibit such a chirality dependence. The stronger the dispersive behavior, the larger is the (n,m) chirality dependence. For this reason, SWNTs with smaller d_t show larger frequency splittings and larger G′-band shift effects. The (n,m) dependence of other combination modes, such as the iTO+LA combination mode near the Γ point, have also been studied in some detail (see e.g. Ref. [227]).

Downloaded by [Shenzhen University Town] at 19:33 15 August 2011

5.6. *Near-field Raman spectroscopy*

The near-field technique can generate optical information with spatial resolution Δx below the diffraction limit ($\Delta x \sim \lambda_{\text{laser}}/2$) [381,382]. The near-field Raman spectroscopy and imaging of individual isolated SWNTs with a record spatial resolution of 25 nm was first measured by Hartschuh *et al.* [382]. In sequence, this group performed several studies of local variations in the Raman spectrum along a single SWNT [45]. Figure 76 shows near-field spectra and imaging for an individual SWNT [293]. In particular, Figure 76(a) and (b) show the photoluminescence and Raman spectra, respectively, with $\Delta x \sim 30$ nm. The near-field microscopy maps from the same SWNT are shown in Figure 76(c)–(f). Figure 76(c) represents the near-field photoluminescence image of this same SWNT, where the image contrast is provided by spectral integration over the photoluminescence peak centered at $\lambda_{\text{em}} = 900$ nm (see Figure 76(a)). The most striking feature in this image is the high degree of spatial localization of the photoluminescence emission along the SWNT. This is evident by inspection of the extended topography image of the nanotube shown in Figure 76(f), and also of the near-field Raman image of the G-band, with a peak intensity near 1590 cm^{-1} shown in Figure 76(d). While from Figure 76(d) we observe that the G band Raman scattering is present along the entire length of the nanotube, from Figure 76(e) we observe an increased defect-induced D band occurring at 1300 cm^{-1}). The strong Raman scattering intensity appears to be localized in the *same* spectral region where exciton emission was detected [387]. Defects are known to act as trapping states for e–h recombination (i.e., exciton emission), thereby providing insights into the correlations observed between Figure 76(c) and (a).

Interestingly, when measuring the Raman spectra across the defective spot, sudden changes in many Raman features are observed. Maciel *et al.* [293] have shown that substitutional doping in SWNTs causes changes in the G′-band spectra due to charge-induced renormalization of the electronic and vibrational energies. Figure 76(g) shows six G′-band spectra measured on the same SWNT, and these spectra were taken by moving along the SWNT to the position where the local D band and photoluminescence emission is observed (circle in Figure 76(e)). The two spectra marked by "*" in Figure 76(g) were obtained at this defect location, and a new peak is here observed in the G′-band. The frequency and intensity of this new peak depend on the dopant species and the level of doping, respectively [383–385]. This makes the G′-band a sensitive probe for studying and quantifying doping, which is more accurate than the D band, since the D-band can also be related to amorphous carbon and to any other symmetry-breaking defective sp^2 structure [193,293,383–385]. Tip-enhanced Raman spectra can show changes in chirality along a given tube [388], due to a large increase in the local signal intensity [389].

6. Challenges of Raman spectroscopy in graphene and carbon nanotubes

We identify in this concluding section current research opportunities where graphene and carbon nanotubes can have special impact. New research areas can be related to new structures, such as nanoribbons, and also to still poorly developed but promising experimental techniques. For example, near-field and time-dependent phenomena have thus far received little attention and show promise for future in-depth development. All these developments have been the basis for the nanometrology field, which is at an early stage of development, and carbon nanotubes have been a focal point for nanometrological protocol development. Although much progress has been made in the use of Raman spectroscopy to study graphene and carbon nanotubes, many research opportunities remain, especially in the applications area. In identifying future directions we look for both novelty and areas of special opportunity, as discussed below.

6.1. *The novelties of graphene*

As already pointed out in this article, graphene appears as the simplest prototype material for solid state physics, let alone the simplest in the family of sp^2 carbons. We still expect a lot more to come with the advance of all kinds of technologies for processing multi-layer graphene samples with different stacking orders, and for generating new kinds of ribbons, edges and defects in general. Here, the technology for producing new kinds of samples is the key issue.

When thinking about the future of graphene nanoribbons, we can now give attention to the past developments of the nanotube field. The great rush into carbon nanotube photophysics arrived when nanotubes with diameters close to 1 nm in diameter and smaller were first produced. Lots of interesting many-body and quantum confinement effects could then be studied in depth, while for larger diameter nanotubes such effects were not so evident. The new physics learned here was then extended to larger diameter tubes. A 1 nm diameter nanotube corresponds to a nanoribbon of about 3–4 nm in width. Since this size is still very small for present technology, we can expect, by analogy, that the most interesting effects are yet to come from nanoribbons smaller than 10 nm in width.

Of course this is not considering edges, which are very interesting by themselves. New and important physics and chemistry related to edges may also come, and these are also dependent on developing more control over the geometry and quality of the edges. For example, the scattering at the edge becomes very important for optics and spin (or charge) transport. Progress has been made, but not enough to lay a strong foundation for the full development of this new research area.

The study of defects in general is a very open field that might generate important new results, both from the study of isolated defects using Raman spectroscopy, as well as through the use of multiple characterization tools that complement Raman spectroscopy. No one has ever measured the characteristic spectral response from a single 7-5-5-7 defect, or from a single vacancy, or even a double vacancy, etc. It is only recently that L_ϕ, the spatial extent of a point-defect induced Raman scattering process ($L_\phi \sim 2$ nm), was measured as is discussed in Section 4.3.3. Furthermore, L_ϕ is expected to exhibit an important dependence on sample temperature. The study of Raman spectroscopy in the transition from a low defect concentration to a high defect concentration may provide important information on the transition from weak to strong localization. These topics are mainly largely discussed for disordered materials, thus providing experimental information for the development of theories linking these limits in 2D materials to studies in few-layer graphene. Defect physics is certainly one of the most open solid state physics sub-fields and this topic can profit greatly from studies made on nearly perfect and highly controlled 2D graphene systems.

However, the rush into studying graphene is not only because it is a prototype material, but also because of the many fundamental connections that physicists see between graphene and fundamental physics. Regarding graphene transport, the Raman effect probes electrons too far from the Fermi level, thus losing out on the most interesting special properties of the massless electrons very close to the Dirac point [61]. However, recent Raman measurements have probed the low-energy excitation states near the Dirac point by studying phonon softening phenomena (Section 5.4) or electronic Raman spectra [206]. As we develop probes that come closer to the Dirac point, we expect that new physics will emerge [62,72,76–82]. For example, the Klein paradox generates a 100% probability for electron tunneling when there is an electron wavefunction matching that for the hole inside an energy barrier. Due to this property, it was shown that one can modulate the electron velocity by generating a periodic potential in graphene [390]. Such an anisotropy in the electron speed could generate measurable shifts in the G$'$-band frequency, and then Raman spectroscopy could be used to easily quantify aspects of the Klein paradox [76,77,81].

Finally, while many new interesting applications for Raman spectroscopy on graphene will certainly come from the preparation of new related samples, there is still room for the development

Downloaded by [Shenzhen University Town] at 19:33 15 August 2011

Downloaded by [Shenzhen University Town] at 19:33 15 August 2011

of our basic knowledge. For example, our understanding related to the intensity of the DR features is marginal. Also, there is still controversy about the assignment of the 2450 cm^{-1} peak, basically because different DR features fall at this frequency, and it is not clear which of them is responsible for the peak. Of course, the relative intensity for the features related to defects depend on the number of defects. However, the relative intensity of the DR features (even those unrelated to defects) change from sample to sample. Graphene, as the prototype material, may shed light into this and other basic issues related to inelastic light scattering.

6.2. *The novelties of carbon nanotubes*

The Raman spectroscopy study of carbon nanotubes and their photophysics, in general, is much more mature than for graphene, and the well-established physics and experimental techniques for nanotubes have been directly applied to study graphene. In a general sense, carbon nanotubes are much more complex than graphene and thus more rich information about solid-state properties can be obtained as a function of the nanotube structure. Though carbon nanotubes have been studied intensively in the past decade, many open issues still remain. For example, very few works have focused on the spectroscopy of carbon nanotube ends, junctions or defect sites even though such spectra can easily be obtained. Double-wall carbon nanotubes are another class of carbon nanotubes that are extremely rich and have until now only been briefly studied, and triple-wall nanotubes have hardly been studied at all. The interlayer interactions in nanotubes are not so well established as in graphene. One advantage of studying nanotubes is that they have a well-defined structure, specified by two integers (n, m), and that nanotubes have no edge structure except for the ends of a SWNT. Using this advantage, the Raman characterization of SWNTs as a function of (n, m) will provide a family of standards for SWNTs. To establish a worldwide standard should be an important issue for the future large scale use of SWNTs in practical applications.

As a more focused example, despite decades of studies, the many-peak structure of the Raman G-band is still full of effects that are not yet well understood and effects related to doping and strain are only now being studied intensively. Furthermore, the behavior of the G-band spectra upon variation of the excitation light resonance condition is still an open issue.

Carbon nanotubes are also very interesting objects for nano electro-mechanical systems (NEMS) because of their strength and stability. Using their strong optical response at the isolated nanotube level and the very high frequency of the LO and iTO modes, SWNTs can be used as very sensitive probes for electronic and structural changes in NEMS. In this sense, carbon nanotubes have already become a prototype material for the development of nanometrology. The importance of carbon nanotubes for applications is already a well-established goal [20], and here Raman spectroscopy could play a very important role as a characterization tool of the changes to the SWNT caused by external perturbations, due to the high degree of accuracy of Raman spectroscopy as a characterization tool along with the relative simplicity of its use for the characterization of carbon nanotube-based materials as a non-contact, non-destructive, room temperature measurement.

The development of standard materials based on carbon nanotubes would be of extreme importance, not only for applications, but also to establish a sensitive probe of various types of SWNT environments. The National Institute of Standards of Technology (NIST, USA) has already developed a round robin program for the measurements of the (n, m) content in a SWNT sample based on the CoMoCAT material [391]. The water-assisted CVD-grown carbon nanotubes (called "super-growth" tubes in the literature [316]) exhibit some results based on their Raman spectra which indicate that this is a special material that is closest to what is expected from a pristine SWNT (isolated from any environmental effect). These special properties are: (1) the special relation between its ω_{RBM} and tube diameter, (2) the highest measured energy for its optical transitions,

Downloaded by [Shenzhen University Town] at 19:33 15 August 2011

and (3) the observation of previously elusive transitions from metallic nanotubes [230]. However, it is not yet clear why this sample is special. Clarifying such a result could help in developing an effective standard reference material in the graphene area.

6.3. *Near-field Raman spectroscopy and microscopy*

The fiber-probe-based near-field systems have the potential for high spatial resolution (50–100 nm) and for the observation of photophysical phenomena in nanostructures. These systems thus far have been largely utilized for luminescence studies, but have hardly given any results on Raman spectroscopy. The near-field Raman spectroscopy and microscopy based on the tip-enhanced Raman scattering (TERS) effect first appeared in 2003 and this work had a strong impact on the photophysics field with the earliest TERS measurements on carbon nanotubes [381,382], and finally achieved a record spatial resolution of 12 nm [45]. However, the instrumentation behind this technique is still very complicated and the developments that have been achieved thus far are still carried out by very few groups in the world. Some companies are starting to produce and sell TERS systems, but the reliability of these systems is not yet in place. Once this technique becomes routine, there is no doubt about its importance to the future development of the Raman spectroscopy field as applied to nano-science. The study of subjects such as isolated defects and edges using TERS is expected to achieve a new paradigm in the near future, which will advance both science and technology.

6.4. *Time-dependent Raman and coherent phonon spectroscopy*

As pointed out in Section 2.3.6, the Fourier transformation of CP vibrations gives a spectrum that is similar to ordinary Raman spectra. It is important to note that CP spectroscopy is not just an alternative tool to Raman spectroscopy, but it is a special tool in its own right that allows observation of the phase of the vibration by which the information about the adiabatic potential for the excited states can be obtained. For example, the RBM vibration starts by opening or closing the nanotube diameter depending of the type (Type I or Type II) of semiconducting SWNTs under investigation [165]. Further, by using pulse-shaping techniques in which the frequency of the repeated laser pulse can be matched to the RBM frequency of a particular SWNT, the CP spectra only for the SWNT can be obtained among the several resonant nanotubes matched to E_{laser}.

The fast response of the transport properties in graphene is now operating in the 100 GHz range [392]. Soon this frequency will become similar to the sp^2 carbon phonon vibration frequency (47 THz for the G-band). In the near future, we may be able to directly observe each physical process contributing to the el–ph interaction and this will help us identify the energy-transfer mechanism in these optical processes. The development of attosecond lasers might bring time-dependent Raman spectroscopy to the level of this newly opened field in which specific electron–electron interactions can also be observed as a function of time.

6.5. *Conclusion and messages for the future*

The developments of Raman spectroscopy as applied to carbon nanotubes and graphene in the past decade has been truly impressive. To demonstrate this, one could develop an interesting set of lectures for a course in solid-state physics by just addressing the Raman spectroscopy on sp^2 carbon systems [1]. The level of information and details that have become available has allowed the development of a very accurate theory to describe the behavior of electrons and phonons in these systems. In this process, Raman spectroscopy has become a widely used tool for the characterization of nanomaterials. This may be the beginning of a new era where information about many-body effects and complex systems will start to be obtained with much better accuracies for

Downloaded by [Shenzhen University Town] at 19:33 15 August 2011

the development of new theories to explain the newly found effects. Raman spectroscopy thus helps the development of nanotechnology in its most basic sense, and allows study of physical processes that are expected to occur at the nanometer level. In following the words of Professor Richard Feynman in his lecture on 29 December 1959, that there is plenty of room for discovery at the bottom, below 10 nm spatial resolution, below 1 meV energy resolution and below 10 fs time resolution, and for the operation of materials at more than 1 THz frequency, 1000 T magnetic field, and 1 TPa pressure.

Acknowledgements

The MIT authors acknowledge the support under NSF Grant DMR 10-04147. A.J. acknowledges the financial support from the Brazilian agencies CNPq, CAPES and FAPEMIG. R.S. acknowledges a Grant-in-Aid (No. 20241023) from the MEXT, Japan. We would like to thank the referee for his/her suggestions which improved the quality of this publication.

For all figures reprinted from American Physical Society material readers may view, browse, and/or download material for temporary copying purposes only, provided these uses are for non-commercial personal purposes. Except as provided by law, this material may not be further reproduced, distributed, transmitted, modified, adapted, performed, displayed, published, or sold in whole or part, without prior written permission from the American Physical Society.

Notes

1. The B atom in Figure 1 gives a brighter STM images than the A atom, since there are electronic energy bands for the B atom near the Fermi energy.
2. The G′ peak in the Raman spectra of sp^2 carbons is often called the 2D peak. It should be noted that the mechanisms involved in the 2D double resonance (DR) processes are different from those for the G′ peak which involves only two phonons. The G′ peak involves only two K point phonons, whereas the 2D feature arises from the second-order D that includes a DR D-band process involving a K point phonon and an elastic scattering process. In this review, we distinguish between the G′ and the 2D scattering process and the actual values of their frequencies.
3. A Stokes process is a terminology used to denote the loss of photon energy in a scattering process. Here the Stokes photoluminescence process is independent of the Stokes Raman process.
4. Time-dependent perturbation theory tells us that the amplitude of the wavefunctions for excited states oscillates as a function of time if the photon energy does not match the excited-state energy, which is the physical meaning of a virtual transition.
5. A notch filter is an optical filter that suppresses a specified range of energies of the incident light.
6. By connecting monochromators in a serial way, the resolution of a monochromator is significantly improved although the actual signal becomes increasingly weak. Furthermore, extra monochromators can be used as an energy-tunable filter to reject the elastically scattered light in contrast to the notch filters, which are wavelength-specific.
7. The solution of a forced damped harmonic oscillator is not generally a Lorentzian lineshape but approaches the Lorentzian function for $\omega_q \gg \Gamma_q$. However, if ω_q approaches Γ_q, the lineshape departs from a Lorentzian function.
8. The designation π of the π band comes from its value of angular momentum which is 1.
9. Here mod denotes an integer function for evaluating the modulus for an (n, m) SWNT where we use the notation mod $(6, 3) = 0$, mod $(7, 3) = 1$ and mod $(8, 3) = 2$ as an illustrative example. Some authors use Mod 1 and Mod 2 to denote a semiconducting nanotube depending on mod$(n - m, 3) = 1$ or 2. There is thus a one-to-one correspondence between type I (II) and Mod 2 (1) semiconducting nanotubes appearing in the literature, and this is clarified in Figure 11.
10. It should be noted that there is a logarithmic 2D van Hove singularity in the density of states of graphene at the saddle point of the energy band near the M points (center of the hexagonal edges) of the BZ.

11. In time-dependent perturbation theory, the mixing (or transition) of the excited states occurs as a function of time with some finite and often measurable probability. The virtual states are defined by such a linear combination of excited states with some probability. The probability for the occupation of an excited state can be large when the energy difference between the excited states and the energy of the external field is relatively small. In such a case, we can say that the transition is resonant with the excited state.
12. Here “real absorption” means that the photo-excited electron can be in the excited states for a sufficient time, for example, 1 ns, so that the electron can be probed in the excited state. A material can scatter photons in a virtual process.
13. It is noted that not all even (odd) vibration modes under inversion symmetry are Raman (IR)-active modes.
14. The two-phonon process involving one-phonon emission and one-phonon absorption does not contribute to the Raman spectra but rather gives a correction to the effective Rayleigh spectral process.
15. Here q is the real phonon wavevector, measured from the Γ point, while in defining q_{DR}, the k and k' vectors are measured from the K point or alternatively, with respect to the K' point.
16. It is only when crystalline disorder is present that the first-order $q \neq 0$ phonons can be observed, as discussed in Section 4.3.
17. From the matrix element $\vec{\alpha}_{\mathrm{p}}$, we can deduce another matrix element,

$$\begin{aligned}\vec{\beta}_{\mathrm{p}}(\tau) &= \int \phi_{\mu}(\mathbf{r})\nabla v(\mathbf{r}-\boldsymbol{\tau})\phi_{\nu}(\mathbf{r}-\boldsymbol{\tau})\,\mathrm{d}\mathbf{r} \\ &= \int \phi_{\nu}(\mathbf{r})\nabla v(\mathbf{r})\phi_{\mu}(\mathbf{r}+\boldsymbol{\tau})\,\mathrm{d}\mathbf{r} = \beta_{\mathrm{p}}(\tau)\hat{I}(\beta_{\mathrm{p}}).\end{aligned} \tag{45a}$$

    However, the integral in Equation (45a) can also be expressed by α terms [268].
18. The phonon amplitude is proportional to $A_{\nu}(\mathbf{q})\sqrt{\bar{n}_{\nu}(\mathbf{q})}$ in which the temperature dependence of the amplitude is expressed by $\bar{n}_{\nu}(\mathbf{q})$ given by Equation (47).
19. It is noted that the minus sign corresponds to a symmetric wavefunction and that the plus sign corresponds to an anti-symmetric wavefunction.
20. A virtual state is a linear combination of real states. When a virtual state is close to an exciton state, the virtual state contains a large component of the exciton states. This is the reason for the approximation used in obtaining a representation for the virtual state.
21. A cutting line is defined by the 1D BZ of an SWNT in the 2D BZ of graphene [32,135,136].
22. Other formula for ω_{RBM} can be used here, too. The difference is within 1–3 cm^{-1}.
23. The subscript htt in T_{htt} denotes heat treatment temperature.
24. Here core electrons refer to 1s and σ electrons. The screening by π electrons is independently considered by the polarization function within the RPA (random phase approximation) [120,148]. See Section 5.2.1 for further details.
25. The Bethe–Salpeter equation is independently solved for each value of κ. When we obtain E_{ii} values as a function of κ by solving the Bethe–Salpeter equation many times, then E_{ii} with different i values are adapted from the different κ value. Since the E_{ii} eigenvalues come from different cutting lines, there is no problem with the orthogonality of the wavefunctions.

References

[1] A. Jorio, R. Saito, G. Dresselhaus, and M.S. Dresselhaus, *Raman Spectroscopy in Graphene Related Systems*, Wiley-VCH Verlag GmbH & Co KGaA, Weinheim, Germany, 2010.
[2] B.T. Kelly, *Physics of Graphite*, Applied Science Publishers, London and New Jersey, 1981, p. 477.
[3] M.M. Lucchese, F. Stavale, E.H. Martins Ferreira, C. Vilani, M.V.O. Moutinho, R.B. Capaz, C.A. Achete, and A. Jorio, Carbon 48(5) (2010), pp. 1592–1597.
[4] L.M. Malard, M.H.D. Guimarães, D.L. Mafra, M.S.C. Mazzoni, and A. Jorio, Phys. Rev. B 79, (2009) p. 125426.
[5] L.M. Malard, M.A. Pimenta, G. Dresselhaus, and M.S. Dresselhaus, Phys. Rep. 473 (2009), pp. 51–87.
[6] R.W.G. Wyckoff, *Crystal Structures*, Wiley, 1963. Vol 6.

Downloaded by [Shenzhen University Town] at 19:33 15 August 2011

Downloaded by [Shenzhen University Town] at 19:33 15 August 2011

[7] K.S. Novoselov, A.K. Geim, S.V. Morozov, D. Jiang, Y. Zhang, S.V. Dubonos, I.V. Grigorieva, and A.A. Firsov, Science 306(5696) (2004), p. 666.

[8] A.K. Geim and A.H. MacDonald, Phys. Today 60(35) (2007), p. 35.

[9] H. Lipson and A.R. Stokes, Nature 149(3777) (1942), p. 328.

[10] A.W. Moore, *Highly Oriented Pyrolytic Graphite*, Vol. 11. Marcel Dekker, New York, 1973.

[11] J. Heremans, C.H. Olk, G.L. Eesley, J. Steinbeck, and G. Dresselhaus, Phys. Rev. Lett. 60 (1988), p. 452,

[12] A.W. Moore, Nature 221(5186) (1969), pp. 1133–1134.

[13] A.W. Moore, *Chemistry and Physics of Carbon*, Vol. 17. Marcel Dekker, New York, 1981.

[14] A.W. Moore, A.R. Ubbelohde, and D.A. Young, Br. J. Appl. Phys. 13 (1962), p. 393.

[15] A.R. Ubbelohde, Carbon 7(5) (1969), pp. 523–530.

[16] I.L. Spain, A.R. Ubbelohde, and D.A. Young, Phil. Trans. R. Soc. London Ser. A, Math. Phys. Sci. 262(1128) (1967), pp. 345–386.

[17] R. Bacon, J. Appl. Phys. 31(2) (1960), p. 283.

[18] M. Endo, T. Koyama, and Y. Hishiyama, Jpn. J. Appl. Phys. 15 (1976), pp. 2073–2076.

[19] M.S. Dresselhaus, G. Dresselhaus, and K. Sugihara, *Graphite Fibers and Filaments* 5. *Springer Series in Materials Science*, Springer, Berlin, 1988.

[20] M. Endo, M.S. Strano, and P.M. Ajayan, *Carbon Nanotubes: Advanced Topics in the Synthesis, Structure, Properties and Applications*, Vol. 111, Springer, Berlin, 2008.

[21] A. Jorio, M.S. Dresselhaus, and G. Dresselhaus, *Carbon Nanotubes: Advanced Topics in the Synthesis, Structure, Properties and Applications*, Vol. 111, Springer, Berlin, 2008.

[22] H.W. Kroto, J.R. Heath, S.C. O'Brien, R.F. Curl, and R.E. Smalley, Nature 318(6042) (1985), pp. 162–163.

[23] M.S. Dresselhaus, G. Dresselhaus, and P.C. Eklund, *Science of Fullerenes and Carbon Nanotubes*, Academic Press, New York, NY/San Diego, CA, 1996.

[24] S. Iijima, Nature 354 (1991), pp. 56–58.

[25] A. Oberlin, M. Endo, and T. Koyama, Carbon 14(2) (1976), pp. 133–135.

[26] A. Oberlin and T. Endo, J. Cryst. Growth 32(3) (1976), pp. 335–349.

[27] A. Oberlin, Carbon 22 (1984), p. 521.

[28] L.V. Radushkevich and V.M. Lukyanovich, Zurn Fisic Chim. 26 (1952), pp. 88–95.

[29] M. Monthioux and V.L. Kuznetsov, Carbon 44 (2006), pp. 1621–1623.

[30] S. Iijima and T. Ichihashi, Nature 363(6430) (1993), pp. 603–605.

[31] D.S. Bethune, C.H. Klang, M.S. De Vries, G. Gorman, R. Savoy, J. Vazquez, and R. Beyers, Nature 363 (1993), p. 605.

[32] R. Saito, G. Dresselhaus, and M.S. Dresselhaus, *Physical Properties of Carbon Nanotubes*, Imperial College Press, London, 1998. London.

[33] S. Reich, C. Thomsen, and P. Ordejon, *Elastic Properties and Pressure-induced Phase Transitions of Single-walled Carbon Nanotubes*, Vol. 235, Wiley Online Library, 2003.

[34] E. Joselevich, H. Dai, J. Liu, K. Hata, and A.H. Windle, *Carbon Nanotubes: Advanced Topics in the Synthesis, Structure, Properties and Applications*, Vol. 111, Springer, Berlin, 2008, pp. 101–164.

[35] M.S. Arnold, A.A. Green, J.F. Hulvat, S.I. Stupp, and M.C. Hersam, Nat. Nanotechnol. 1(1) (2006), pp. 60–65.

[36] M. Terrones, A.G. Souza Filho, and A.M. Rao, *Carbon Nanotubes: Advanced Topics in the Synthesis, Structure, Properties and Applications*, Vol. 111, Springer, Berlin, 2008, pp. 531–566.

[37] M. Yudasaka, S. Iijima, and V.H. Crespi, *Carbon Nanotubes: Advanced Topics in the Synthesis, Structure, Properties and Applications*, Vol. 111, Springer, Berlin, 2008, pp. 605–629.

[38] B.I. Yakobson, Appl. Phys. Lett. 72(8) (1998), p. 918.

[39] C.D. Spataru, S. Ismail-Beigi, R. Capaz, and S.G. Louie, *Carbon Nanotubes: Advanced Topics in the Synthesis, Structure, Properties and Applications*, Vol. 111, Springer, Berlin, 2008, pp. 195–228.

[40] T. Ando, *Carbon Nanotubes: Advanced Topics in the Synthesis, Structure, Properties and Applications*, Vol. 111, Springer, Berlin, 2008, pp. 229–250.

[41] R. Saito, C. Fantini, and J. Jiang, *Carbon Nanotubes: Advanced Topics in the Synthesis, Structure, Properties and Applications*, Vol. 111, Springer, Berlin, 2008, pp. 251–286.

Downloaded by [Shenzhen University Town] at 19:33 15 August 2011

[42] J. Lefebvre, S. Maruyama, and P. Finnie, *Carbon Nanotubes: Advanced Topics in the Synthesis, Structure, Properties and Applications*, Vol. 111, Springer, Berlin, 2008, pp. 287–319.

[43] Y.-Z. Ma, T. Hertel, Z.V. Vardeny, G.R. Fleming, and L. Valkunas, *Carbon Nanotubes: Advanced Topics in the Synthesis, Structure, Properties and Applications*, Vol. 111, Springer, Berlin, 2008, pp. 321–352.

[44] T.F. Heinz, *Carbon Nanotubes: Advanced Topics in the Synthesis, Structure, Properties and Applications*, Vol. 111, Springer, Berlin, 2008, pp. 353–369.

[45] A. Hartschuh, *Carbon Nanotubes: Advanced Topics in the Synthesis, Structure, Properties and Applications*, Vol. 111, Springer, Berlin, 2008, pp. 371–392.

[46] J. Kono, J.R. Nicholas, and S. Roche, *Carbon Nanotubes: Advanced Topics in the Synthesis, Structure, Properties and Applications*, Vol. 111, Springer, Berlin, 2008, pp. 393–421.

[47] P. Avouris, M. Freitag, and V. Perebeinos, *Carbon Nanotubes: Advanced Topics in the Synthesis, Structure, Properties and Applications*, Vol. 111, Springer, Berlin, 2008, pp. 423–454.

[48] J. Wu, W. Walukiewicz, W. Shan, E. Bourret-Courchesne, J.W. Ager III, K.M. Yu, E.E. Haller, K. Kissell, S.M. Bachilo, and R.B. Weisman, Phys. Rev. Lett. 93(1) (2004), p. 17404.

[49] M.S. Biercuk, S. Ilani, and C.M. Marcus, *Carbon Nanotubes: Advanced Topics in the Synthesis, Structure, Properties and Applications*, Vol. 111, Springer, Berlin, 2008, pp. 455–492.

[50] L. Kavan and L. Dunsch, *Carbon Nanotubes: Advanced Topics in the Synthesis, Structure, Properties and Applications*, Vol. 111, Springer, Berlin, 2008, pp. 567–603.

[51] M. Kalbac, H. Farhat, L. Kavan, J. Kong, and M.S. Dresselhaus, Nano Lett. 8(10) (2008), pp. 3532–3537.

[52] P.R. Wallace, Phys. Rev. 71(9) (1947), pp. 622–634.

[53] H.P. Boehm, A. Clauss, U. Hofmann, and G.O. Fischer, Z. Naturforschung B 17(3) (1962), p. 150.

[54] A.M. Affoune, B.L.V. Prasad, H. Sato, T. Enoki, Y. Kaburagi, and Y. Hishiyama, Chem. Phys. Lett. 348(1–2) (2001), pp. 17–20.

[55] C. Berger, Z. Song, T. Li, X. Li, A.Y. Ogbazghi, R. Feng, Z. Dai, A.N. Marchenkov, E.H. Conrad, P.N. First, and W.A. de Heer, J. Phys. Chem. B 108(52) (2004), pp. 19912–19916.

[56] T. Enoki, Y. Kobayashi, C. Katsuyama, V.Y. Osipov, M.V. Baidakova, K. Takai, K.I. Fukui, and A.Y. Vul, Diam. Relat. Mater. 16(12) (2007), pp. 2029–2034.

[57] Y. Kobayashi, K. Fukui, T. Enoki, K. Kusakabe, and Y. Kaburagi, Phys. Rev. B 71(19) (2005), p. 193406.

[58] Y. Kobayashi, K. Fukui, T. Enoki, and K. Kusakabe, Phys. Rev. B 73(12) (2006), p. 125415.

[59] L.G. Cancado, M.A. Pimenta, B.R.A. Neves, G. Medeiros-Ribeiro, T. Enoki, Y. Kobayashi, K. Takai, K. Fukui, M.S. Dresselhaus, and R. Saito, Phys. Rev. Lett. 93(4) (2004), p. 47403.

[60] A.K. Geim and K.S. Novoselov, Nat. Mater. 6(3) (2007), pp. 183–191.

[61] A. Castro Neto, F. Guinea, N.M.R. Peres, K.S. Novoselov, and A.K. Geim, Rev. Mod. Phys. 81(1) (2009), pp. 109–162.

[62] M.S. Dresselhaus and P.T. Araujo, ACS Nano 4(11) (2010), pp. 6297–6302.

[63] C. Lee, X. Wei, J.W. Kysar, and J. Hone, Science 321(5887) (2008), p. 385.

[64] A.A. Balandin and O.L. Lazarenkova, Appl. Phys. Lett. 82 (2003), p. 415.

[65] D. Teweldebrhan and A.A. Balandin, Appl. Phys. Lett. 94 (2009), p. 13101.

[66] K.I. Bolotin, K.J. Sikes, Z. Jiang, M. Klima, G. Fudenberg, J. Hone, P. Kim, and H.L. Stormer, Solid State Commun. 146(9–10) (2008), pp. 351–355.

[67] S. Morozov, K. Novoselov, M. Katsnelson, F. Schedin, D. Elias, J. Jaszczak, and A. Geim, Phys. Rev. Lett. 100(1) (2008), p. 16602.

[68] B. Lee, Y. Chen, F. Duerr, D. Mastrogiovanni, E. Garfunkel, E.Y. Andrei, and V. Podzorov, Nano Lett. 10 (2010), pp. 1407–1433.

[69] X. Du, I. Skachko, A. Barker, and E.Y. Andrei, Nat. Nanotechnol. 3(8) (2008), pp. 491–495.

[70] G. Li and E.Y. Andrei, Nat. Phys. 3 (2007), p. 623.

[71] X. Du, I. Skachko, F. Duerr, A. Luican, and E.Y. Andrei, Nature 462 (2009), pp. 192–195.

[72] K.S. Novoselov, A.K. Geim, S.V. Morozov, D. Jiang, M.I. Katsnelson, I.V. Grigorieva, S.V. Dubonos, and A.A. Firsov, Nature 438(7065) (2005), pp. 197–200.

[73] K.S. Novoselov, E. McCann, S.V. Morozov, V.I. Fal'ko, M.I. Katsnelson, U. Zeitler, D. Jiang, F. Schedin, and A.K. Geim, Nat. Phys. 2(3) (2006), pp. 177–180.

[74] R.R. Nair, P. Blake, A.N. Grigorenko, K.S. Novoselov, T.J. Booth, T. Stauber, N.M.R. Peres, and A.K. Geim, Science (New York) 320(5881) (2008), p. 1308.
[75] A.F. Young and P. Kim, Nat. Phys. 5(3) (2009), pp. 222–226.
[76] C.W.J. Beenakker, Rev. Mod. Phys. 80(4) (2008), pp. 1337–1354.
[77] M.I. Katsnelson, K.S. Novoselov, and A.K. Geim, Nat. Phys. 2(9) (2006), pp. 620–625.
[78] V.V. Cheianov, V. Fal'ko, and B.L. Altshuler, Science 315(5816) (2007), pp. 1252–1255.
[79] J.M. Pereira Jr., V. Mlinar, F.M. Peeters, and P. Vasilopoulos, Phys. Rev. B 74(4) (2006), p. 45424.
[80] V. Cheianov and V. Fal'ko, Phys. Rev. B 74(4) (2006), p. 041403.
[81] C.W.J. Beenakker, Phys. Rev. Lett. 97(6) (2006), p. 67007.
[82] F. Miao, S. Wijeratne, Y. Zhang, U.C. Coskun, W. Bao, and C.N. Lau, Science 317(5844) (2007), pp. 1530–1533.
[83] A. Ossipov, M. Titov, and C. Beenakker, Phys. Rev. B 75(24) (2007), p. 241401.
[84] C. Beenakker, A. Akhmerov, P. Recher, and J. Tworzydlo, Phys. Rev. B 77(7) (2008), p. 075409.
[85] T. Pedersen, C. Flindt, J. Pedersen, N. Mortensen, A.-P. Jauho, and K. Pedersen, Phys. Rev. Lett. 100(13) (2008), p. 136804.
[86] J.S. Park, K. Sasaki, R. Saito, W. Izumida, M. Kalbac, H. Farhat, G. Dresselhaus, and M.S. Dresselhaus, Phys. Rev. B 80(8) (2009), p. 81402.
[87] D.C. Elias, R.R. Nair, T.M.G. Mohiuddin, S.V. Morozov, P. Blake, M.P. Halsall, A.C. Ferrari, D.W. Boukhvalov, M.I. Katsnelson, and A.K. Geim, Science 323(5914) (2009), p. 610.
[88] A.K. Geim, Science (New York) 324(5934) (2009), pp. 1530–1534.
[89] C. Berger, Z. Song, X. Li, X. Wu, N. Brown, C. Naud, D. Mayou, T. Li, J. Hass, A.N. Marchenkov, E.H. Conrad, P.N. First, and W.A. de Heer, Electronic confinement and coherence in patterned epitaxial graphene, Since 312, 1191–1196 (2006).
[90] X. Li, X. Wang, L. Zhang, S. Lee, and H. Dai, Science 319(5867) (2008), p. 1229.
[91] X. Yang, X. Dou, A. Rouhanipour, L. Zhi, H.J. Räder, and K. Müllen, J. Am. Chem. Soc. 130(13) (2008), pp. 4216–4217.
[92] D.V. Kosynkin, A.L. Higginbotham, A. Sinitskii, J.R. Lomeda, A. Dimiev, B.K. Price, and J.M. Tour, Nature 458(7240) (2009), pp. 872–876.
[93] L. Jiao, L. Zhang, X. Wang, G. Diankov, and H. Dai, Nature 458(7240) (2009), pp. 877–880.
[94] X. Jia, M. Hofmann, V. Meunier, B.G. Sumpter, J. Campos-Delgado, J.M. Romo-Herrera, H. Son, Y.-P. Hsieh, A. Reina, J. Kong, M. Terrones, and M.S. Dresselhaus, Science 323 (2009), pp. 1701–1705.
[95] M. Cardona, in *Light Scattering in Solids II*, M. Cardona and G. Güntherodt, eds., Vol. 50, Springer, Berlin, 1982, pp. 19–176.
[96] M.S. Dresselhaus, A. Jorio, M. Hofmann, G. Dresselhaus, and R. Saito, Nano Lett. 10 (2010), pp. 953–973.
[97] A.C. Ferrari, Raman spectroscopy of graphene and graphite: disorder, electron–phonon coupling, doping and nonadiabatic effects, July 2007. Solid State Communications, 143 (2007), pp. 47–57.
[98] D. Haberer, D.V. Vyalikh, S. Taioli, B. Dora, M. Farjam, J. Fink, D. Marchenko, T. Pichler, K. Ziegler, S. Simonucci, M.S. Dresselhaus, M. Knupfer, B. Büchner, and A. Grüneis, Nano Lett. 10 (2010), pp. 3360–3366.
[99] M.S. Dresselhaus, G. Dresselhaus, and R. Saito, Phys. Rev. B 45(11) (1992), pp. 6234–6242.
[100] R. Saito, T. Takeya, T. Kimura, G. Dresselhaus, and M.S. Dresselhaus, Phys. Rev. B 57(7) (1998), pp. 4145–4153.
[101] E.B. Barros, N. Demir, A.G. Souza Filho, J. Mendes Filho, A. Jorio, G. Dresselhaus, and M.S. Dresselhaus, Phys. Rev. B 71(16), 2005.
[102] F. Tuinstra and J.L. Koenig, J. Chem. Phys. 53(3) (1970), p. 1126.
[103] A.M. Rao, E. Richter, S. Bandow, B. Chase, P.C. Eklund, K.A. Williams, S. Fang, K.R. Subbaswamy, M. Menon, A. Thess, R.E. Smalley, G. Dresselhaus, and M.S. Dresselhaus, Science 275(5297) (1997), pp. 187–191.
[104] C. Thomsen and S. Reich, Phys. Rev. Lett. 85(24) (2000), pp. 5214–5217.
[105] L. Alvarez, A. Righi, T. Guillard, S. Rols, E. Anglaret, D. Laplaze, and J.L. Sauvajol, Chem. Phys. Lett. 316(3–4) (2000), pp. 186–190.

Downloaded by [Shenzhen University Town] at 19:33 15 August 2011

[106] H. Kuzmany, W. Plank, M. Hulman, Ch. Kramberger, A. Grüneis, Th. Pichler, H. Peterlik, H. Kataura, and Y. Achiba, Eur. Phys. J. B 22(3) (2001), pp. 307–320.

[107] H. Telg, J. Maultzsch, S. Reich, F. Hennrich, and C. Thomsen, Phys. Rev. Lett. 93 (2004), p. 177401.

[108] J. Meyer, M. Paillet, T. Michel, A. Moréac, A. Neumann, G. Duesberg, S. Roth, and J.-L. Sauvajol, Phys. Rev. Lett. 95(21) (2005), p. 217401.

[109] M. Milnera, J. Kürti, M. Hulman, and H. Kuzmany, Phys. Rev. Lett. 84(6) (2000), pp. 1324–1327.

[110] S. Lefrant, J.P. Buisson, J. Schreiber, O. Chauvet, M. Baibarac, and I. Baltog, Synth. Met. 139(3) (2003), pp. 783–785.

[111] A. Jorio, R. Saito, J. Hafner, C. Lieber, M. Hunter, T. McClure, G. Dresselhaus, and M.S. Dresselhaus, Phys. Rev. Lett. 86(6) (2001), pp. 1118–1121.

[112] A.C. Ferrari, J. Meyer, V. Scardaci, C. Casiraghi, M. Lazzeri, F. Mauri, S. Piscanec, D. Jiang, K. Novoselov, S. Roth, and A. Geim, Phys. Rev. Lett. 97(18) (2006), p. 187401.

[113] D. Graf, F. Molitor, K. Ensslin, C. Stampfer, A. Jungen, C. Hierold, and L. Wirtz, Nano Lett. 7(2) (2007), pp. 238–242.

[114] A. Gupta, G. Chen, P. Joshi, S. Tadigadapa, and P.C. Eklund, Nano Lett. 6(12) (2006), pp. 2667–2673.

[115] K. Sasaki, R. Saito, M.S. Dresselhaus, K. Wakabayashi, T. Enoki, New J. Phys. 12 (2010), p. 103015.

[116] C.V. Raman and K.S. Krishnan, Nature 121(3048) (1928), p. 501.

[117] G. Landsberg and L. Mandelstam, Naturwissenschaften 16 (1928), pp. 772–772.

[118] F. Bassani, G. Pastori Parravicini, and R.A. Ballinger, *Electronic States and Optical Transitions in Solids*, Pergamon Press, New York, 1975.

[119] N.W. Ashcroft and N.D. Mermin, *Solid State Physics*, Holt, Rinehart and Winston, New York, 1976.

[120] T. Ando, J. Phys. Soc. Jpn. 66(4) (1997), pp. 1066–1073.

[121] F. Wang, G. Dukovic, L.E. Brus, and T.F. Heinz, Science 308(5723) (2005), p. 838.

[122] J. Maultzsch, R. Pomraenke, S. Reich, E. Chang, D. Prezzi, A. Ruini, E. Molinari, M.S. Strano, C. Thomsen, and C. Lienau, Phys. Rev. B 72(24) (2005), p. 241402.

[123] S.Y. Zhou, G.-H. Gweon, J. Graf, A.V. Fedorov, C.D. Spataru, R.D. Diehl, Y. Kopelevich, D.-H. Lee, S.G. Louie, and A. Lanzara, Nat. Phys. 2(9) (2006), pp. 595–599.

[124] A. Bostwick, T. Ohta, T. Seyller, K. Horn, and E. Rotenberg, Nat. Phys. 3(1) (2006), pp. 36–40.

[125] A. Grüneis, C. Attaccalite, T. Pichler, V. Zabolotnyy, H. Shiozawa, S. Molodtsov, D. Inosov, A. Koitzsch, M. Knupfer, J. Schiessling, R. Follath, R. Weber, P. Rudolf, L. Wirtz, and A. Rubio, Phys. Rev. Lett. 100(3) (2008), p. 37601.

[126] K. Sugawara, T. Sato, S. Souma, T. Takahashi, and H. Suematsu, Phys. Rev. Lett. 98(3) (2007), p. 36801.

[127] W. Kohn, Phys. Rev. Lett. 2 (1959), p. 393.

[128] S.D.M. Brown, A. Jorio, P. Corio, M.S. Dresselhaus, G. Dresselhaus, R. Saito, and K. Kneipp, Phys. Rev. B 63(15) (2001), p. 155414.

[129] U. Fano, Phys. Rev. 124(6) (1961), pp. 1866–1878.

[130] E.H. Martins Ferreira, M.V.O. Moutinho, F. Stavale, M.M. Lucchese, R.B. Capaz, C.A. Achete, and A. Jorio, Phys. Rev. B 82(12) (2010), p. 125429.

[131] A.C. Ferrari and J. Robertson, Phys. Rev. B 61(20) (2000), pp. 14095–14107.

[132] R.J. Nemanich, S.A. Solin, and R.M. Martin, Phys. Rev. B 23(12) (1981), pp. 6348–6356.

[133] H. Richter, Z.P. Wang, and L. Ley, Solid State Commun. 39(5) (1981), pp. 625–629.

[134] I.H. Campbell and P.M. Fauchet, Solid State Commun. 58(10) (1986), pp. 739–741.

[135] G.G. Samsonidze, R. Saito, A. Jorio, M.A. Pimenta, A.G. Souza Filho, A. Grüneis, G. Dresselhaus, and M.S. Dresselhaus, J. Nanosci. Nanotechnol. 3(6) (2003), pp. 431–458.

[136] R. Saito, K. Sato, Y. Oyama, J. Jiang, G.G. Samsonidze, G. Dresselhaus, and M.S. Dresselhaus, Phys. Rev. B 71 (2005), p. 153413.

[137] M.S. Dresselhaus, G. Dresselhaus, A.M. Rao, A. Jorio, A.G. Souza Filho, G.G. Samsonidze, and R. Saito, Indian J. Phys. 77B (2003), pp. 75–99.

[138] R. Saito, J. Jiang, A. Grüneis, K. Sato, Y. Oyama, G.G. Samsonidze, S.G. Chou, G. Dresselhaus, M.S. Dresselhaus, L.G. Cançado, C. Fantini, A. Jorio, and M.A. Pimenta, Mol. Cryst. Liquid Cryst. 455 (2006), pp. 287–294.

Downloaded by [Shenzhen University Town] at 19:33 15 August 2011

Downloaded by [Shenzhen University Town] at 19:33 15 August 2011

[139] J. Jiang, R. Saito, A. Grüneis, S.G. Chou, G.G. Samsonidze, A. Jorio, G. Dresselhaus, and M.S. Dresselhaus, Phys. Rev. B 71 (2005), pp. 45417–45419.

[140] K. Nakada, M. Fujita, G. Dresselhaus, and M.S. Dresselhaus, Phys. Rev. B 54 (1996), pp. 17954–17961.

[141] S. Reich, C. Thomsen, and J. Maultzsch, *Carbon Nanotubes, Basic Concepts and Physical Properties*, Wiley-VCH, Berlin, 2004.

[142] E.B. Barros, A. Jorio, G.G. Samsonidze, R.B. Capaz, A.G. Souza Filho, J. Mendes Filho, G. Dresselhaus, and M.S. Dresselhaus, Phys. Rep. 431(6) (2006), pp. 261–302.

[143] Y.W. Son, M.L. Cohen, and S.G. Louie, Phys. Rev. Lett. 97(21) (2006), p. 216803.

[144] Y.W. Son, M.L. Cohen, and S.G. Louie, Nature 444(7117) (2006), pp. 347–349.

[145] J. Maultzsch, S. Reich, and C. Thomsen, Raman scattering in carbon nanotubes revisited, Phys. Rev. B 65 (2002), p. 3402.

[146] H. Telg, J. Maultzsch, S. Reich, and C. Thomsen, Phys. Rev. B 74(11) (2006), p. 115415.

[147] C.D. Spataru, S. Ismail-Beigi, L.X. Benedict, and S.G. Louie, Phys. Rev. Lett. 92(7) (2004), p. 77402.

[148] J. Jiang, R. Saito, G.G. Samsonidze, A. Jorio, S.G. Chou, G. Dresselhaus, and M.S. Dresselhaus, Phys. Rev. B 75 (2007), pp. 35407–35413.

[149] V.G. Kravets, A.N. Grigorenko, R.R. Nair, P. Blake, S. Anissimova, K.S. Novoselov, and A.K. Geim, Phys. Rev. B 81(15) (2010), p. 155413.

[150] M.Y. Sfeir, T. Beetz, F. Wang, L. Huang, X.M. Henry Huang, M. Huang, J. Hone, S. O'Brien, J.A. Misewich, T.F. Heinz, L. Wu, Y. Zhu, and L.E. Brus, Science 312(5773) (2006), pp. 554–556.

[151] C. Casiraghi, A. Hartschuh, H. Qian, S. Piscanec, C. Georgi, A. Fasoli, K.S. Novoselov, D.M. Basko, and A.C. Ferrari, Nano Lett. 9(4) (2009), pp. 1433–1441.

[152] M.J. O'Connell, S.M. Bachilo, C.B. Huffman, V.C. Moore, M.S. Strano, E.H. Haroz, K.L. Rialon, P.J. Boul, W.H. Noon, and C. Kittrell, Science 297(5581) (2002), p. 593.

[153] S.M. Bachilo, L. Balzano, J.E. Herrera, F. Pompeo, D.E. Resasco, and R. Bruce Weisman, J. Am. Chem. Soc. 125(37) (2003), pp. 11186–11187.

[154] S.G. Chou, F. Plentz, J. Jiang, R. Saito, D. Nezich, H.B. Ribeiro, A. Jorio, M.A. Pimenta, G.G. Samsonidze, and A.P. Santos, Phys. Rev. Lett. 94(12) (2005), p. 127402.

[155] R.C.C. Leite and S.P.S. Porto, Phys. Rev. Lett. 17(1) (1966), pp. 10–12.

[156] M. Freitag, J. Chen, J. Tersoff, J.C. Tsang, Q. Fu, J. Liu, and Ph. Avouris, Phys. Rev. Lett. 93(7) (2004), p. 76803.

[157] S. Essig, C.W. Marquardt, A. Vijayaraghavan, M. Ganzhorn, S. Dehm, F. Hennrich, F. Ou, A.A. Green, C. Sciascia, F. Bonaccorso, K.-P. Bohnen, H.v. Lohneysen, M.M. Kappes, P.M. Ajayan, M.C. Hersam, A.C. Ferrari, and R. Krupke, Nano Lett. 10 (2010), p. 1589.

[158] Y. Chen, R.C. Haddon, S. Fang, A.M. Rao, P.C. Eklund, W.H. Lee, E.C. Dickey, E.A. Grulke, J.C. Pendergrass, and A. Chavan, J. Mater. Res. 13(9) (1998), pp. 2423–2431.

[159] U.J. Kim, C.A. Furtado, X. Liu, G. Chen, and P.C. Eklund, J. Am. Chem. Soc. 127(44) (2005), pp. 15437–15445.

[160] J. Kastner, T. Pichler, H. Kuzmany, S. Curran, W. Blau, D.N. Weldon, M. Delamesiere, S. Draper, and H. Zandbergen, Chem. Phys. Lett. 221(1–2) (1994), pp. 53–58.

[161] A. Gambetta, C. Manzoni, E. Menna, M. Meneghetti, G. Cerullo, G. Lanzani, S. Tretiak, A. Piryatinski, A. Saxena, and R.L. Martin, Nat. Phys. 2(8) (2006), pp. 515–520.

[162] Y.-S. Lim, K.-J. Yee, J.-H. Kim, E.H. Hároz, J. Shaver, J. Kono, S.K. Doorn, R.H. Hauge, and R.E Smalley, Nano Lett. 6(12) (2006), pp. 2696–2700.

[163] K. Ishioka, M. Hase, M. Kitajima, L. Wirtz, A. Rubio, and H. Petek, Phys. Rev. B 77 (2008), p. 121402(R).

[164] K. Kato, K. Ishioka, M. Kitajima, J. Tang, R. Saito, and H. Petek, Nano Lett. 8(10) (2008), pp. 3102–3108.

[165] A. Jones, A. Ballestad, T. Li, M. Whitwick, J. Rottler, and T. Tiedje, Phys. Rev. B 79(20) (2009), pp. 205419–205434.

[166] K.S. Krishnan and C.V. Raman, Proc. R. Soc. Lond. Ser. A 115(772) (1927), pp. 549–554.

[167] M.S. Dresselhaus, G. Dresselhaus, R. Saito, and A. Jorio, *Raman Spectroscopy of Carbon Nanotubes*, Vol. 409, Elsevier, the Netherlands, 2005.

[168] J. Klett, R. Hardy, E. Romine, C. Walls, and T. Burchell, Carbon 38(7) (2000), pp. 953–973.

[169] A.C. Ferrari and J. Robertson, Phil. Trans. R. Soc. Lond. A 362 (2004), pp. 2477–2512.

[170] L.G. Cançado, M.A. Pimenta, B.R.A. Neves, M.S.S. Dantas, and A. Jorio, Phys. Rev. Lett. 93, 247401 (2004).

[171] A. Jorio, A.G. Souza Filho, G. Dresselhaus, M.S. Dresselhaus, A. Swan, M. Ünlü, B. Goldberg, M.A. Pimenta, J. Hafner, C.M. Lieber, and R. Saito, Phys. Rev. B 65(15) (2002), p. 155412.

[172] A.C. Ferrari and J. Robertson, Phys. Rev. B 64(7) (2001), p. 75414.

[173] M.J. Pelletier, *Analytical Applications of Raman Spectroscopy*, Wiley-Blackwell, Oxford, UK, 1999, p. 478.

[174] M.A. Pimenta, G. Dresselhaus, M.S. Dresselhaus, L.G. Cancado, A. Jorio, and R. Saito, Phys. Chem. Chem. Phys. 9(11) (2007), pp. 1276–1290.

[175] C. Fantini, A. Jorio, M. Souza, M.S. Strano, M.S. Dresselhaus, and M.A. Pimenta, Phys. Rev. Lett. 93(14) (2004), p. 147406.

[176] Y. Kumazawa, H. Kataura, Y. Maniwa, I. Umezu, S. Suzuki, Y. Ohtsuka, and Y. Achiba, Synth. Met. 103(1–3) (1999), pp. 2555–2558.

[177] R. Saito, G. Dresselhaus, and M.S. Dresselhaus, Phys. Rev. B 61 (2000), pp. 2981–2990.

[178] A.M. Rao, P.C. Eklund, S. Bandow, A. Thess, and R.E. Smalley, Nature 388(6639) (1997), pp. 257–259.

[179] K. Kneipp, H. Kneipp, P. Corio, S. Brown, K. Shafer, J. Motz, L. Perelman, E. Hanlon, A. Marucci, G. Dresselhaus, and M.S. Dresselhaus, Phys. Rev. Lett. 84(15) (2000), pp. 3470–3473.

[180] P. Corio, S.D.M. Brown, A. Marucci, M.A. Pimenta, K. Kneipp, G. Dresselhaus, and M.S. Dresselhaus, Phys. Rev. B 61(19) (2000), pp. 13202–13211.

[181] S. Lefrant, Curr. Appl. Phys. 2(6) (2002), pp. 479–482.

[182] K. Kneipp, A. Jorio, H. Kneipp, S. Brown, K. Shafer, J. Motz, R. Saito, G. Dresselhaus, and M.S. Dresselhaus, Phys. Rev. B 63(8) (2001), p. 81401.

[183] G. Goncalves, P.A.A.P. Marques, C.M. Granadeiro, H.I.S. Nogueira, M.K. Singh, and J. Gracio, Chem. Mater. 21(20) (2009), pp. 4796–4802.

[184] L. Gao, W. Ren, B. Liu, R. Saito, Z.-S. Wu, S. Li, C. Jiang, F. Li, and H.-M. Cheng, ACS Nano 3(4) (2009), pp. 933–9.

[185] X. Ling, L. Xie, Y. Fang, H. Xu, H. Zhang, J. Kong, M.S. Dresselhaus, J. Zhang, and Z. Liu, Nano Lett. 10(2) (2010), pp. 553–561.

[186] F. Schedin, E. Lidorikis, A. Lombardo, V.G. Kravetsand, A.K. Geim, A.N. Grigorenko, K.S. Novoselov, and A.C. Ferrari, ACS Nano 4 (2010), p. 5617.

[187] W. Ren, R. Saito, L. Gao, F. Zheng, Z. Wu, B. Liu, M. Furukawa, J. Zhao, Z. Chen, and H.-M. Cheng, Phys. Rev. B 81(3) (2010), p. 35412.

[188] A. Hartschuh, H.N. Pedrosa, L. Novotny, and T.D. Krauss, Science 301(5638) (2003), p. 1354.

[189] K. Ikeda and K. Uosaki, Nano Lett. 9(4) (2009), pp. 1378–1381.

[190] A. Zumbusch, G.R. Holtom, and X. Sunney Xie, Phys. Rev. Lett. 82(20) (1999), pp. 4142–4145.

[191] A. Das, B. Chakraborty, S. Piscanec, S. Pisana, A.K. Sood, and A.C. Ferrari, Phys. Rev. B 79(15) (2009), p. 155417.

[192] L.M. Malard, D.C. Elias, E.S. Alves, and M.A. Pimenta, Phys. Rev. Lett. 101(25) (2008), p. 257401.

[193] S. Piscanec, M. Lazzeri, J. Robertson, A.C. Ferrari, and F. Mauri, Phys. Rev. B 75(3) (2007), p. 35427.

[194] S. Piscanec, M. Lazzeri, F. Mauri, A.C. Ferrari, and J. Robertson, Phys. Rev. Lett. 93(18) (2004), p. 185503.

[195] A. Das, S. Pisana, B. Chakraborty, S. Piscanec, S.K. Saha, U.V. Waghmare, K.S. Novoselov, H.R. Krishnamurthy, A.K. Geim, and A.C. Ferrari, Nature Nanotechnology, 3, 210–215, (2008).

[196] K. Sasaki, R. Saito, G. Dresselhaus, M.S. Dresselhaus, H. Farhat, and J. Kong, Phys. Rev. B 77 (2008), p. 245441.

[197] M. Lazzeri and F. Mauri, Phys. Rev. Lett. 97(26) (2006), p. 266407.

[198] K. Ishikawa and T. Ando, J. Phys. Soc. Jpn. 75(8) (2006), p. 84713.

[199] V.N. Popov and P. Lambin, Phys. Rev. B 73(8) (2006), p. 854635607.

[200] J. Yan, E.A. Henriksen, P. Kim, and A. Pinczuk, Phys. Rev. Lett. 101(13) (2008), p. 136804.

[201] H. Farhat, H. Son, G. Samsonidze, S. Reich, M.S. Dresselhaus, and J. Kong, Phys. Rev. Lett. 99(14) (2007), p. 145506.

Downloaded by [Shenzhen University Town] at 19:33 15 August 2011

Downloaded by [Shenzhen University Town] at 19:33 15 August 2011

[202] M. Kalbac, L. Kavan, H. Farhat, J. Kong, and M.S. Dresselhaus, J. Phys. Chem. C 113(5) (2009), pp. 1751–1757.

[203] M. Kalbac, H. Farhat, L. Kavan, J. Kong, K. Sasaki, R. Saito, and M.S. Dresselhaus, ACS Nano 3 (2009), pp. 2320–2328.

[204] H. Farhat, K. Sasaki, M. Kalbac, M. Hofmann, R. Saito, M.S. Dresselhaus, and J. Kong, Phys. Rev. Lett. 102(12) (2009), pp. 268041–4.

[205] K. Sasaki, H. Farhat, R. Saito, and M.S. Dresselhaus, Phys. E 42(8) (2010), pp. 2005–2015.

[206] H. Farhat, S. Berciaud, M. Kalbac, R. Saito, T. Heinz, M.S. Dresselhaus, and J. Kong, unpublished.

[207] A.V. Baranov, A.N. Bekhterev, Y.S. Bobovich, and V.I. Petrov, Opt. Spectrosc. 62 (1987), pp. 612–616.

[208] J. Maultzsch, S. Reich, and C. Thomsen, Phys. Rev. B 70(15) (2004), p. 155403.

[209] R. Saito, A. Grüneis, G.G. Samsonidze, V.W. Brar, G. Dresselhaus, M.S. Dresselhaus, A. Jorio, L.G. Cançado, C. Fantini, and M.A. Pimenta, New J. Phys. 5 (2003), p. 157.

[210] R. Saito, A. Jorio, A.G. Souza Filho, G. Dresselhaus, M.S. Dresselhaus, and M. Pimenta, Phys. Rev. Lett. 88(2) (2001), p. 27401.

[211] R. Saito, A. Grüneis, L.G. Cançado, M.A. Pimenta, A. Jorio, A.G. Souza Filho, M.S. Dresselhaus, and G. Dresselhaus, Mol. Cryst. Liq. Cryst. 387 (2002), pp. 287–296.

[212] I. Pócsik, M. Hundhausen, M. Koósa, and L. Ley, J. Non-Cryst. Solids 227–230 (1998), pp. 1083–1086.

[213] D. Mafra, G. Samsonidze, L. Malard, D. Elias, J. Brant, F. Plentz, E. Alves, and M. Pimenta, Phys. Rev. B 76(23) (2007) 233407.

[214] R. Vidano and D.B. Fischbach, J. Am. Ceram. Soc. 61(1–2) (1978), pp. 13–17.

[215] R.P. Vidano and L.J. Fischbach, Solid State Commun. 39(2) (1981), pp. 341–344.

[216] L.G. Cançado, M.A. Pimenta, R. Saito, A. Jorio, L.O. Ladeira, A. Grueneis, A.G. Souza-Filho, G. Dresselhaus, and M.S. Dresselhaus, Phys. Rev. B 66(3) (2002), p. 35415.

[217] J. Zimmermann, P. Pavone, and G. Cuniberti, Phys. Rev. B 78(4) (2008), p. 45410.

[218] M. Lazzeri, C. Attaccalite, L. Wirtz, and F. Mauri, Phys. Rev. B 78(8) (2008), p. 81406.

[219] D.M. Basko, Phys. Rev. B 78(11) (2008), p. 115432.

[220] D.M. Basko, S. Piscanec, and A.C. Ferrari, Phys. Rev. B 80(16) (2009), p. 165413.

[221] T. Shimada, T. Sugai, C. Fantini, M. Souza, L.G. Cançado, A. Jorio, M.A. Pimenta, R. Saito, A. Grüneis, and G. Dresselhaus, Carbon 43(5) (2005), pp. 1049–1054.

[222] M.A. Pimenta, E.B. Hanlon, A. Marucci, P. Corio, S.D.M. Brown, S.A. Empedocles, M.G. Bawendi, G. Dresselhaus, and M.S. Dresselhaus, Brazilian J. Phys. 30(2) (2000), pp. 423–427.

[223] R.J. Nemanich and S.A. Solin, Phys. Rev. B 20(2) (1979), pp. 392–401.

[224] P.H. Tan, Y.M. Deng, and Q. Zhao, Phys. Rev. B 58(9) (1998), pp. 5435–5439.

[225] E.F. Atunes, A.O. Lobo, E.J. Corat, V.J. Trava-Airoldi, A.A. Martin, and C. Verissimo, Carbon 44(11) (2006), pp. 2202–2211.

[226] P.H. Tan, C.Y. Hu, J. Dong, W.C. Shen, and B.F. Zhang, Phys. Rev. B 64(21) (2001), p. 214301.

[227] V.W. Brar, G.G. Samsonidze, M.S. Dresselhaus, G. Dresselhaus, R. Saito, A. Swan, M. Ünlü, B. Goldberg, A.G. Souza Filho, and A. Jorio, Phys. Rev. B 66(15) (2002), p. 155418.

[228] M. Pimenta, A. Marucci, S. Empedocles, M. Bawendi, E. Hanlon, A. Rao, P. Eklund, R. Smalley, G. Dresselhaus, and M.S. Dresselhaus, Phys. Rev. B 58(24) (1998), pp. R16016–R16019.

[229] P.T. Araujo, A. Jorio, M.S. Dresselhaus, K. Sato, and R. Saito, Phys. Rev. Lett. 103(14) (2009), p. 146802.

[230] P.T. Araujo, P.B.C. Pesce, M.S. Dresselhaus, K. Sato, R. Saito, and A. Jorio, Phys. E 42 (2010), pp. 1251–1261.

[231] Y. Miyauchi, R. Saito, K. Sato, Y. Ohno, S. Iwasaki, T. Mizutani, J. Jiang, and S. Maruyama, Chem. Phys. Lett. 442(4–6) (2007), pp. 394–399.

[232] A.R.T. Nugraha, R. Saito, K. Sato, P.T. Araujo, A. Jorio, and M.S. Dresselhaus, Appl. Phys. Lett. 97(9) (2010), p. 91905.

[233] K. Sato, R. Saito, Y. Oyama, J. Jing, L.G. Cancado, M.A. Pimenta, A. Jorio, G.G. Samsonidze, G. Dresselhaus, and M.S. Dresselhaus, Chem. Phys. Lett. 427(1–3) (2006), pp. 117–121.

[234] S. Uryu and T. Ando, Phys. Semicond. B 893 (2007), pp. 1033–1034.

[235] R.A. Jishi, L. Venkataraman, M.S. Dresselhaus, and G. Dresselhaus, Chem. Phys. Lett. 209 (1993), pp. 77–82.

[236] R. Nicklow, N. Wakabayashi, and H.G. Smith, Phys. Rev. B 5(12) (1972), pp. 4951–4962.

[237] J.L. Wilkes, R.E. Palmer, and R.F. Willis, J. Electron Spectrosc. Rel. Phenom. 44(1) (1987), pp. 355–360.

[238] T. Aizawa, R. Souda, S. Otani, Y. Ishizawa, and C. Oshima, Phys. Rev. B 42(18) (1990), pp. 11469–11478.

[239] R. Al-Jishi and G. Dresselhaus, Phys. Rev. B 26(8) (1982), pp. 4514–4522.

[240] S. Siebentritt, R. Pues, K.-H. Rieder, and A.M. Shikin, Phys. Rev. B 55(12) (1997), pp. 7927–7934.

[241] C. Mapelli, C. Castiglioni, G. Zerbi, and K. Müllen, Phys. Rev. B 60(18) (1999), pp. 12710–12725.

[242] C.D. Spataru, S. Ismail-Beigi, L.X. Benedict, and S.G. Louie, Appl. Phys. A Mater. Sci. Process. 78(8) (2004), pp. 1129–1136.

[243] R. Saito, A. Jorio, J. Jiang, K. Sasaki, G. Dresselhaus, and M.S. Dresselhaus, *Optical Properties of Carbon Nanotubes and Nanographene*, Oxford University Press, Oxford, UK, 2010.

[244] A. Grüneis, J. Serrano, A. Bosak, M. Lazzeri, S.L. Molodtsov, L. Wirtz, C. Attaccalite, M. Krisch, A. Rubio, F. Mauri, and T. Pichler, Phys. Rev. B 80(8) (2009), p. 85423.

[245] M. Furukawa, Thesis. Master's Thesis, Tohoku University, 2010.

[246] K. Sasaki, M. Yamamoto, S. Murakami, R. Saito, M.S. Dresselhaus, K. Takai, T. Mori, T. Enoki, and K. Wakabayashi, Phys. Rev. B 80(15) 155450 (2009).

[247] N. Mounet and N. Marzari, Phys. Rev. B 71(20) (2005), p. 205214.

[248] D. Sanchez-Portal, E. Artacho, J.M. Solar, A. Rubio, and P. Ordejon, Phys. Rev. B 59 (1999), pp. 12678–12688.

[249] O. Dubay and G. Kresse, Phys. Rev. B 67(3) (2003), p. 35401.

[250] J.-C. Charlier, P. Eklund, J. Zhu, and A.C. Ferrari, *Electron and phonon properties of graphene: their relationship with carbon nanotubes*, Vol. 111, Springer Series on Topics in Applied Physics, Springer, Berlin, 2008, pp. 625–680.

[251] P.H. Tan, L. An, L.Q. Liu, Z.X. Guo, R. Czerw, D.L. Carroll, P.M. Ajayan, N. Zhang, and H.L. Guo, Phys. Rev. B 66(24) (2002), p. 245410.

[252] J. Hone, *Phonons and Thermal Properties of Carbon Nanotubes*, Vol. 80, Springer, Berlin, 2001, pp. 273–286.

[253] D. Porezag, Th. Frauenheim, Th. Köhler, G. Seifert, and R. Kaschner, Phys. Rev. B 51(19) (1995), pp. 12947–12957.

[254] G.G. Samsonidze, R. Saito, N. Kobayashi, A. Grüneis, J. Jiang, A. Jorio, S.G. Chou, G. Dresselhaus, and M.S. Dresselhaus, Appl. Phys. Lett. 85 (2004), pp. 5703–5705.

[255] A. Grüneis, C. Attaccalite, L. Wirtz, H. Shiozawa, R. Saito, T. Pichler, and A. Rubio, Phys. Rev. B 78(20) (2008), p. 205425.

[256] S. Reich, J. Maultzsch, C. Thomsen, and P. Ordejón, Phys. Rev. B 66(3) (2002), p. 35412.

[257] J. Slonczewski and P. Weiss, Phys. Rev. 109(2) (1958), pp. 272–279.

[258] M. Koshino and T. Ando, Phys. Rev. B 77(11) (2008), p. 115313.

[259] J.C. Slater and G.F. Koster, Phys. Rev. 94(6) (1954), pp. 1498–1524.

[260] J.J.P. Stewart, *MOPAC93.00*, Fujitsu Limited, Tokyo, Japan, 1993.

[261] M.J. Frisch, G.W. Trucks, H.B. Schlegel, G.E. Scuseria, M.A. Robb, J.R. Cheeseman, G. Scalmani, V. Barone, B. Mennucci, G.A. Petersson, H. Nakatsuji, M. Caricato, X. Li, H.P. Hratchian, A.F. Izmaylov, J. Bloino, G. Zheng, and D.J. Sonnenb, *Gaussian 09, Revision A.1*, Gaussian, Inc., Wallingford, CT, 2009.

[262] A. Grüneis, R. Saito, G.G. Samsonidze, T. Kimura, M.A. Pimenta, A. Jorio, A.G. Souza Filho, G. Dresselhaus, and M.S. Dresselhaus, Phys. Rev. B 67(16) (2003), pp. 165402–165407.

[263] Y. Oyama, R. Saito, K. Sato, J. Jiang, G.G. Samsonidze, A. Grüneis, Y. Miyauchi, S. Maruyama, A. Jorio, G. Dresselhaus, and M.S. Dresselhaus, Carbon 44(5) (2006), pp. 873–879.

[264] R. Saito, A. Grüneis, G.G. Samsonidze, G. Dresselhaus, M.S. Dresselhaus, A. Jorio, L.G. Cancado, M.A. Pimenta, and A.G. Souza Filho, Appl. Phys. A 78(8) (2004), pp. 1099–1105.

[265] J. Jiang, R. Saito, A. Grüneis, G. Dresselhaus, and M.S. Dresselhaus, Carbon 42 (2004), pp. 3169–3176.

[266] G.G. Samsonidze, E.B. Barros, R. Saito, J. Jiang, G. Dresselhaus, and M.S. Dresselhaus, Phys. Rev. B 75 (2007), p. 155420.

Downloaded by [Shenzhen University Town] at 19:33 15 August 2011

Downloaded by [Shenzhen University Town] at 19:33 15 August 2011

[267] J. Jiang, R. Saito, A. Grüneis, G. Dresselhaus, and M.S. Dresselhaus, Chem. Phys. Lett. 392 (2004), pp. 383–389.

[268] J. Jiang, R. Saito, G.G. Samsonidze, S.G. Chou, A. Jorio, G. Dresselhaus, and M.S. Dresselhaus, Phys. Rev. B 72 (2005), pp. 235408–235411.

[269] J. Jiang, R. Saito, A. Grüneis, S. Chou, G. Samsonidze, A. Jorio, G. Dresselhaus, and M.S. Dresselhaus, Phys. Rev. B 71(20) (2005), p. 205420.

[270] A. Grüneis, *Resonance Raman spectroscopy of single wall carbon nanotubes*, Ph.D. thesis, Tohoku University, Sendai, Japan, September 2004.

[271] R. Saito and H. Kamimura, J. Phys. Soc. Jpn. 52(2) (1983), p. 407.

[272] T. Ando, J. Phys. Soc. Jpn. 74(3) (2005), pp. 777–817.

[273] J. Jiang, R. Saito, K. Sato, J. Park, G.G. Samsonidze, A. Jorio, G. Dresselhaus, and M.S. Dresselhaus, Phys. Rev. B 75(3) (2007), p. 35405.

[274] M. Rohlfing and S.G. Louie, Phys. Rev. B 62(8) (2000), pp. 4927–4944.

[275] V. Perebeinos, J. Tersoff, and P. Avouris, Phys. Rev. Lett. 92(25) (2004), p. 257402.

[276] R.B. Capaz, C. Spataru, S. Ismail-Beigi, and S.G. Louie, Phys. Rev. B 74(12) (2006), pp. 5–8.

[277] E.B. Barros, R.B. Capaz, A. Jorio, G.G. Samsonidze, A.G. Souza Filho, S. Ismail-Beigi, C.D. Spataru, S.G. Louie, G. Dresselhaus, and M.S. Dresselhaus, Phys. Rev. B 73(24) (2006), p. 241406.

[278] J.S. Park, Y. Oyama, R. Saito, W. Izumida, J. Jiang, K. Sato, C. Fantini, A. Jorio, G. Dresselhaus, and M.S. Dresselhaus, Phys. Rev. B 74 (2006), p. 165414.

[279] Z. Yu and L.E. Brus, J. Phys. Chem. B 105(29) (2001), pp. 6831–6837.

[280] S. Reich, C. Thomsen, and P. Ordejón, Phy. Rev. B, 64, (2001) p. 195416.

[281] P.K. Eklund, G. Dresselhaus, M.S. Dresselhaus, and J. Fischer, Phys. Rev. B 16(8) (1977), pp. 3330–3333.

[282] A.W. Bushmaker, V.V. Deshpande, S. Hsieh, M.W. Bockrath, and S.B. Cronin, Nano Lett. 9(8) (2009), pp. 2862–2866.

[283] Y. Wu, J. Maultzsch, E. Knoesel, B. Chandra, M. Huang, M. Sfeir, L.E. Brus, J. Hone, and T.F. Heinz, Phys. Rev. Lett. 99(2) (2007), p. 27402.

[284] L.M. Malard, J. Nilsson, D.C. Elias, J.C. Brant, F. Plentz, E.S. Alves, A.H. Castro-Neto, and M.A. Pimenta, Phys. Rev. B 76(20) (2007), p. 201401.

[285] N. Ferralis, R. Maboudian, and C. Carraro, Phys. Rev. Lett. 101(15) (2008), p. 156801.

[286] T.M.G. Mohiuddin, A. Lombardo, R.R. Nair, A. Bonetti, G. Savini, R. Jalil, N. Bonini, D.M. Basko, C. Galiotis, N. Marzari, K.S. Novoselov, A.K. Geim, and A.C. Ferrari, Phys. Rev. B 79 (2009), p. 205433.

[287] M. Huang, H. Yan, C. Chen, D. Song, T.F. Heinz, and J. Hone, Phonon softening and crystallographic orientation of strained graphene studied by Raman spectroscopy, May 2009.

[288] S. Pisana, M. Lazzeri, C. Casiraghi, K.S. Novoselov, A.K. Geim, A.C. Ferrari, and F. Mauri, Nat. Mater. 6(3) (2007), pp. 198–201.

[289] J. Yan, Y. Zhang, P. Kim, and A. Pinczuk, Phys. Rev. Lett. 98(16) 166802 (2007).

[290] Y. Wang, Z. Ni, T. Yu, Z.X. Shen, H. Wang, Y. Wu, W. Chen, and A.T. Shen Wee, J. Phys. Chem. C 112(29) (2008), pp. 10637–10640.

[291] C. Casiraghi, S. Pisana, K.S. Novoselov, A.K. Geim, and A.C. Ferrari, Appl. Phys. Lett. 91 (2007), p. 233108.

[292] G. Compagnini, F. Giannazzo, S. Sonde, V. Raineri, and E. Rimini, Carbon 47(14) (2009), pp. 3201–3207.

[293] I.O. Maciel, N. Anderson, M.A. Pimenta, A. Hartschuh, H. Qian, M. Terrones, H. Terrones, J. Campos-Delgado, A.M. Rao, L. Novotny, and A. Jorio, Nat. Mater. 7(11) (2008), pp. 878–883.

[294] X. Wang, L. Zhi, and K. Müllen, Nano Lett. 8(1) (2008), pp. 323–327.

[295] Z. Ni, Y. Wang, T. Yu, Y. You, and Z. Shen, Phys. Rev. B 77(23) (2008), p. 235403.

[296] D.M. Basko, Phys. Rev. B 76(8) (2007), p. 81405.

[297] J.S. Park, A. Reina Cecco, R. Saito, J. Jiang, G. Dresselhaus, and M.S. Dresselhaus, Carbon 47 (2009), pp. 1303–1310.

[298] L.G. Cançado, A. Reina, J. Kong, and M.S. Dresselhaus, Phys. Rev. B 77(24) (2008), p. 245408.

[299] P. Lespade, A. Marchand, M. Couzi, and F. Cruege, Carbon 22(4–5) (1984), pp. 375–385.

[300] P. Lespade, R. Al-Jishi, and M.S. Dresselhaus, Carbon 20(5) (1982), pp. 427–431.

[301] H. Wilhelm, M. Lelaurain, E. McRae, and B. Humbert, J. Appl. Phys. 84 (1998), p. 6552.

[302] R.J. Nemanich and S.A. Lucovsky, Solid State Commun. 23(2) (1977), pp. 117–120.

[303] L.G. Cancado, K. Takai, T. Enoki, M. Endo, Y.A. Kim, H. Mizusaki, A. Jorio, L.N. Coelho, R. Magalhaes-Paniago, and M.A. Pimenta, Appl. Phys. Lett. 88(16) (2006), p. 163106.

[304] P. Poncharal, A. Ayari, T. Michel, and J.L. Sauvajol, Phys. Rev. B 79(19) (2009), p. 195417.

[305] A. Reina, H.B. Son, L.Y. Jiao, B. Fan, M.S. Dresselhaus, Z.F. Liu, and J. Kong, J. Phys. Chem. C 112(46) (2008), pp. 17741–17744.

[306] A. Reina, S. Thiele, X. Jia, S. Bhaviripudi, M.S. Dresselhaus, J.A. Schaefer, and J. Kong, Nano Res. 2 (2009), pp. 509–516.

[307] C.H. Lui, Z. Li, Z. Chen, P.V. Klimov, L.E. Brus, and T.F. Heinz, Nano Lett. 11(1) (2011), pp. 164–169.

[308] M.S. Dresselhaus and R. Kalish, *Ion Implantation in Diamond, Graphite and Related Materials*, Springer Series in Materials Science, Springer, Berlin, 1992.

[309] A. Jorio, M.M. Lucchese, F. Stavale, E.H. Martins Ferreira, M.V.O. Moutinho, R.B. Capaz, and C.A. Achete, J. Phys.: Condens. Matter 22(33) (2010), p. 334204.

[310] A. Grüneis, R. Saito, T. Kimura, L.G. Cançado, M.A. Pimenta, A. Jorio, A.G. Souza Filho, G. Dresselhaus, and M.S. Dresselhaus, Phys. Rev. B 65(15) (2002), pp. 155405–155407.

[311] A.K. Gupta, T.J. Russin, H.R. Gutierrez, and P.C. Eklund, ACS Nano 3 (2009), pp. 45–52.

[312] B. Krauss, P. Nemes-Incze, V. Skakalova, L.P. Biro, K. von Klitzing, and J.H. Smet, Nano Lett. (11)(10) (2010), pp. 4544–4548.

[313] M.S. Dresselhaus, G. Dresselhaus, and A. Jorio, J. Phys. Chem. C 111 (2007), pp. 17887–17893.

[314] P.T. Araujo, I.O. Maciel, P.B.C. Pesce, M.A. Pimenta, S.K. Doorn, H. Qian, A. Hartschuh, M. Steiner, L. Grigorian, and K. Hata, Phys. Rev. B 77(24) (2008), p. 241403.

[315] G.D. Mahan, Phys. Rev. B 65(23) (2002), p. 235402.

[316] K. Hata, D.N. Futaba, K. Mizuno, T. Namai, M. Yumura, and S. Iijima, Science 306(5700) (2004), p. 1362.

[317] S.M. Bachilo, M.S. Strano, C. Kittrell, R.H. Hauge, R.E. Smalley, and R.B. Weisman, Science 298(5602) (2002), p. 2361.

[318] M.S. Strano, J. Am. Chem. Soc. 125(51) (2003), pp. 16148–16153.

[319] S.K. Doorn, D.A. Heller, P.W. Barone, M.L. Usrey, and M.S. Strano, Appl. Phys. A 78(8) (2004), pp. 1147–1155.

[320] T. Michel, M. Paillet, P. Poncharal, A. Zahab, J.-L. Sauvajol, J.C. Meyer, and S. Roth, Carbon Nanotubes 222(II) (2006), pp. 121–122.

[321] P.T. Araujo, S.K. Doorn, S. Kilina, S. Tretiak, E. Einarsson, S. Maruyama, H. Chacham, M.A. Pimenta, and A. Jorio, Phys. Rev. Lett. 98(6) (2007), p. 67401.

[322] P.T. Araujo, C. Fantini, M.M. Lucchese, M.S. Dresselhaus, and A. Jorio, Appl. Phys. Lett. 95(26) (2009), p. 261902.

[323] J.S. Soares, L.G. Cançado, E.B. Barros, and A. Jorio, Phys. Stat. Solidi B 247(11–12) (2010), pp. 2835–2837.

[324] J.S. Soares, A.P.M. Barboza, P.T. Araujo, N.M. Barbosa Neto, D. Nakabayashi, N. Shadmi, T.S. Yarden, A. Ismach, N. Geblinger, E. Joselevich, C. Vilani, L.G. Cancado, L. Novotny, G. Dresselhaus, M.S. Dresselhaus, B.R.A. Neves, M.S.C. Mazzoni, and A. Jorio, Nano Lett. 10(12) (2010), pp. 5043–5048.

[325] R. Pfeiffer, C. Kramberger, F. Simon, H. Kuzmany, V.N. Popov, and H. Kataura, Eur. Phys. J. B 42(3) (2004), pp. 345–350.

[326] R. Pfeiffer, F. Simon, H. Kuzmany, and V.N. Popov, Phys. Rev. B 72(16) (2005), p. 161404.

[327] R. Pfeiffer, F. Simon, H. Kuzmany, V.N. Popov, V. Zolyomi, and J. Kurti, Phys. Stat. Solidi B 243(13) (2006), pp. 3268–3272.

[328] R. Pfeiffer, H. Peterlik, H. Kuzmany, F. Simon, K. Pressl, P. Knoll, M.H. Rümmeli, H. Shiozawa, H. Muramatsu, Y.A. Kim, T. Hayashi, and M. Endo, Phys. Stat. Solidi B 245(10) (2008), pp. 1943–1946.

[329] H. Kuzmany, W. Plank, R. Pfeiffer, and F. Simon, J. Raman Spectrosc. 39(2) (2008), pp. 134–140.

[330] F. Villalpando-Paez, H. Muramatsu, Y.A. Kim, H. Farhat, M. Endo, M. Terrones, and M.S. Dresselhaus, Nanoscale 2(3) (2010), pp. 406–411.

[331] F. Villalpando-Paez, H. Son, D. Nezich, Y.P. Hsieh, J. Kong, Y.A. Kim, D. Shimamoto, H. Muramatsu, T. Hayashi, M. Endo, M. Terrones, and M.S. Dresselhaus, Nano Lett. 8 (2008), pp. 3879–3886.

Downloaded by [Shenzhen University Town] at 19:33 15 August 2011